Seasonal Modulation of Dissolved Oxygen in the Equatorial Pacific by Tropical Instability Vortices

Y. A. Eddebbar[1*], A. C. Subramanian[2], D. B. Whitt[3,4], M. C. Long[3], A. Verdy[1], M. R. Mazloff[1], and M. A. Merrifield[1]

[1]Scripps Institution of Oceanography, University of California, San Diego, La Jolla, CA 92037, USA
[2]Atmospheric and Oceanic Sciences, Colorado University, Boulder, CO 80309, USA
[3]Climate and Global Dynamics, National Center for Atmospheric Research, Boulder, CO 80305, USA
[4]NASA Ames Research Center, Moffett Field, CA 94035, USA

Key Points:

- Tropical Instability Vortices (TIVs) oxygenate the northern upper equatorial Pacific
- TIVs seasonality modulates the Oxygen Minimum Zone (OMZ) structure and seasonal variability of ecosystem habitable space in the equatorial Pacific
- TIVs' oxygenation is driven largely by eddy advective effects

*9500 Gilman Dr., La Jolla, CA

Corresponding author: Yassir Eddebbar, `yeddebba@ucsd.edu`

Abstract

Tropical Instability Vortices (TIVs) have a major influence on the physics and biogeochemistry of the equatorial Pacific. Using an eddy-resolving configuration of the Community Earth System Model (CESM-HR) and Lagrangian particle tracking, we examine TIV impacts on the three-dimensional structure and variability of dissolved oxygen (O_2) in the upper equatorial Pacific water column. In CESM-HR, the simulated generation and westward propagation of TIVs from boreal summer through winter lead to the seasonal oxygenation of the upper northern equatorial Pacific, exhibited as a deepening of hypoxic depth west of 120°W. TIV effects on the equatorial Pacific oxygen balance are dominated by eddy-advection and mixing, while indirect TIV effects on O_2 consumption play minor roles. These advective effects reflect the transient displacements of isopycnals by eddy pumping as well as vortex transport of oxygen by eddy trapping, stirring, and subduction. TIVs influence on the upper equatorial Pacific O_2 distribution and variability has important implications for understanding and modeling marine ecosystem dynamics and habitats, and should be taken into consideration in designing observation networks in this region.

Plain Language Summary

Tropical Instability Vortices (TIVs) are eddies that stir and transport water masses in the equatorial Pacific. From summer through winter, vortices are generated in the eastern equatorial Pacific and propagate towards the west, causing major physical and biogeochemical changes in the upper equatorial Pacific. We examine their effects on oxygen distributions and variability in the equatorial Pacific using a global model of ocean circulation and biogeochemistry. From boreal summer through winter, TIVs oxygenate the upper ocean through a series of processes, namely their influence on upper ocean density layers and lateral and vertical water mass exchanges that lead to a temporary deepening of the oxygen minimum zones and an expansion of vertical habitable space along their paths. Our analysis demonstrates that TIVs comprise an important mechanism regulating simulated oxygen distributions in the equatorial Pacific; these important phenomena should be explored in observational campaigns and their effects should be considered in the context of improving climate models.

1 Introduction

The equatorial Pacific is home to rich biodiversity and abundant fisheries. A major control on marine ecosystem habitable space in this region is the presence of the tropical Pacific Oxygen Minimum Zones (OMZs), where marine life is severely limited by hypoxic (O_2 <60 mmol.m^{-3}) conditions (Vaquer-Sunyer & Duarte, 2008; Gallo & Levin, 2016; Deutsch et al., 2020). Observations indicate a concerning decline in the global ocean O_2 content associated with anthropogenic warming in recent decades (Keeling et al., 2010; Ito et al., 2017), with the equatorial Pacific accounting for the highest regional contribution to the globally integrated O_2 change (Schmidtko et al., 2017). A mechanistic explanation for the equatorial Pacific O_2 decline, exhibited as an expansion of the tropical Pacific OMZs (Stramma, Schmidtko, et al., 2010), however, remains out of reach, hindered by incomplete understanding and poor model representation of processes governing the O_2 balance in this region (Cabré et al., 2015; Brandt et al., 2015). Characterizing these processes is critical to modeling marine biogeochemical and ecosystem dynamics in the tropical Pacific and predicting their future in a warming climate (Lehodey et al., 2010, 2013; Mislan et al., 2017).

OMZs result from poor ventilation and microbial O_2 consumption at depth (Sverdrup, 1938; Wyrtki, 1962). They are typically found in eastern tropical regions, where equatorward O_2 supply by the ventilated thermocline is restricted (Luyten et al., 1983), and where productivity along the eastern boundary upwelling systems (EBUS) fuels microbial respiration at depth (Karstensen et al., 2008). The eastern north and south tropical Pacific OMZs are two of the world's largest (Karstensen et al., 2008), and are separated by an equatorial oxygenated tongue (EOT) set by vigorous O_2 supply from the western Pacific through the equatorial current system (Stramma, Johnson, et al., 2010), particularly by the Equatorial Undercurrent (EUC) (Busecke et al., 2019) and the North and South Subsurface Countercurrents (NSCC and SSCC) (Margolskee et al., 2019). Due to their coarse configurations, models do not represent these advective pathways well and thus generate OMZs that are too extensive, challenging the fidelity of their future projections (Duteil et al., 2014; Cabré et al., 2015; Busecke et al., 2019; Kwiatkowski et al., 2020). Further, the role of mesoscale (10-100km) eddies on the OMZs structure and variability is not well understood (Brandt et al., 2015), and their parameterization by coarse models may further contribute to the large O_2 biases exhibited in this region. Identifying the role of mesoscale circulation on O_2 distribution and supply in the upper equatorial Pacific has important implications for predicting the fate of the OMZs in a warming world.

Mesoscale eddies have been suggested to have a major influence on O_2 distribution and variability in the upper ocean, both through physical eddy transport as well as their indirect impacts on biogeochemistry (Bettencourt et al., 2015; Thomsen et al., 2016). A regional model simulation of the northern Indian Ocean, for instance, showed that vertical and lateral eddy supply of O_2 acts to reduce the Arabian Sea OMZ extent (Resplandy et al., 2012). In the eastern north tropical Atlantic, however, glider observations of anticyclonic modewater eddies (ACMEs) show nearly anoxic ($O_2 = 0$ mmol.m^{-3}) conditions within the eddy cores (Karstensen et al., 2015). Throughout their westward translation from their EBUS origin, these low-O_2 ACMEs showcase complex biogeochemical feedbacks by intensifying nutrient supply and productivity that amplify microbial O_2 consumption in the well-isolated eddy core (Schütte et al., 2016; Karstensen et al., 2017). A global eddy-resolving model study (Frenger et al., 2018) illustrated the basin scale O_2 imprints of these ACMEs as "hypoxic cannon balls" that export low-O_2 undercurrent waters from EBUS regions into the subtropical gyres interior. While mesoscale eddy effects on OMZs along EBUS have generated substantial interest in recent years, little is known about their roles along the equatorial Pacific, where the baroclinic Rossby radius of deformation is larger (Chelton et al., 1998) and where tropical instability vortices (TIVs) dominate the eddy kinetic energy field (Ubelmann & Fu, 2011; Zheng et al., 2016).

TIVs are large anticyclonic eddies that are associated with the more widely known Tropical Instability Waves (TIWs) (Flament et al., 1996; Kennan & Flament, 2000). They propagate westward at speeds of about 0.30 m s^{-1} along the equatorial Pacific and Atlantic, with eddy cores centered around 5°N and diameters of about 500 km (Kennan & Flament, 2000; Menkes et al., 2002). TIVs arise from barotropic and baroclinic instabilities generated by the shear between the North Equatorial Counter Current (NECC), the South Equatorial Current (SEC) and the EUC (Philander, 1976; Cox, 1980). TIV activity is strongly seasonal, with vortex generation typically developing in boreal summer and subsiding by winter (Willett et al., 2006; Zheng et al., 2016; Wang et al., 2019). Throughout their westward propagation, TIVs exhibit a complex 3D circulation characterized by strong anticyclonic flow and vigorous downwelling and upwelling along their leading and trailing edges, respectively, associated with frontogenesis (Kennan & Flament, 2000; Dutrieux et al., 2008; Holmes et al., 2014).

TIV imprints on the equatorial Pacific are visible from space as a train of undulating sea surface temperature (SST) fronts (Kennan & Flament, 2000), and play an important role in modulating the equatorial mixed layer heat balance (Menkes et al., 2006; Moum et al., 2009), turbulent mixing (Lien et al., 2008; Holmes & Thomas, 2015; Inoue et al., 2019; Cherian et al., 2021), and ENSO dynamics (Holmes et al., 2019). TIVs also exert a profound influence on biogeochemistry through modulating nutrient transport, plankton distributions, and carbon export (Archer et al., 1997; Strutton et al., 2001;

Menkes et al., 2002; Dunne et al., 2000; Gorgues et al., 2005), setting up hot spots of primary productivity that attract large concentrations of tuna fisheries and other megafauna (Morlière et al., 1994; Ménard et al., 2000; Ryan et al., 2017).

TIVs showcase long lifetimes (>2 months) with observed impacts on circulation throughout the upper 200 m of the northern equatorial Pacific (Ubelmann & Fu, 2011; Flament et al., 1996; Menkes et al., 2002). TIVs anticyclonic flow induces a substantial vertical displacement of isopycnal surfaces through "eddy pumping" (Holmes et al., 2014; McGillicuddy, 2016), with potential impacts on hypoxic depth. This anticyclonic flow may also smooth out the pronounced lateral gradients in O_2 through "eddy stirring" effects (Dutrieux et al., 2008; McGillicuddy, 2016). The intense rotational velocities exhibited by TIVs can also trap water masses (Dutrieux et al., 2008), which can be zonally advected by the TIVs westward propagation, a process known as "eddy trapping". Finally, the intense downwelling and upwelling velocities reported along the leading and trailing edges of TIVs may lead to the "subduction" of surface waters along sloping isopycnals to depth (Holmes et al., 2014) and exposure of low-O_2 thermocline waters to the surface, respectively. Given the shallow depth (100-200 m) of hypoxic conditions bounding the OMZ and the pronounced lateral and vertical O_2 gradients that characterize the upper eastern and central equatorial Pacific, these TIV-induced physical and biogeochemical changes may have a large influence on the O_2 distribution and balance in this region, with potential implications for understanding OMZ dynamics and O_2 biases in climate models.

Here, we use a global eddy-resolving model of ocean circulation and biogeochemistry to study the effects of TIVs on O_2 distribution and variability in the upper equatorial Pacific, and examine the physical and biogeochemical mechanisms governing these effects. In section 2, we describe our modeling and analysis methods. We evaluate the model representation of equatorial Pacific circulation and oxygen distribution in Section 3. In section 4, we examine the simulated imprints of TIVs on oxygen distribution and assess seasonal aspects of these TIV effects in section 5. Section 6 explores the mechanisms governing these effects using an analysis of the oxygen balance and Lagrangian particle tracking. Finally, we conclude with a summary and discussion of our findings in section 7.

2 Methods

2.1 CESM Experiments

We use an eddy-resolving configuration of the ocean and sea-ice components of the Community Earth System Model version 1 (CESM1) (Hurrell et al., 2013) to understand TIV effects on equatorial Pacific O_2. The ocean is simulated with the Parallel Ocean Program version 2 (POP2) (Smith et al., 2010) using the "0.1°" nominal resolution configuration (Small et al., 2014; Harrison et al., 2018), referred to herein as CESM-HR, with a horizontal grid resolution of about 11 km in the equatorial region. The vertical grid contains 62 levels, spaced at 10 m in the upper 160 m, and increasing to 250m in the deeper ocean. Vertical mixing in POP2 is represented following the K-profile parameterization (KPP) scheme (W. G. Large et al., 1994).

Ocean biogeochemistry is represented by the Biogeochemical Elemental Cycle (BEC) model (Moore et al., 2013), where lower trophic ecosystem dynamics are simulated using the nutrient-phytoplankton-zooplankton-detritus paradigm, including light and nutrient co-limitation (N, P, Si, and Fe), three functional groups (diatoms, diazotrophs, and pico/nano phytoplankton), an implicit calcifier group, and a zooplankton group (Moore et al., 2013; Long et al., 2013). Global and regional simulations of BEC have been widely conducted and validated against observations (Moore et al., 2013; Long et al., 2013, 2016), including with the eddy-resolving configuration used in this study (Harrison et al., 2018).

Analog simulations of CESM1 at the "1°" nominal non-eddying resolution, with a refined resolution of about 30 km in latitude by 125 km in longitude near the equator, are used to evaluate the impact of model resolution on simulating equatorial Pacific circulation and O_2 distribution. At this lower resolution, referred to herein as CESM-LR, the model uses the Gent-McWilliams mesoscale eddy parameterization scheme (Gent & Mcwilliams, 1990) and Redi scheme for isopycnal mixing (Redi, 1982) with time-varying diffusivities, and parameterizes the restratification effects of submesoscale instabilities in the surface mixed layer (Fox-Kemper et al., 2011). Both configurations employ the KPP vertical mixing scheme (W. G. Large et al., 1994), though CESM-HR explicitly resolves the effects of mesoscale eddies, does not parameterize the restratification effects of submesoscale instabilities in the mixed layer, and only uses biharmonic diffusion as a lateral closure for the tracers and momentum budgets.

We use a hindcast of the ocean-ice system forced by a repeating annual climatological cycle of the atmosphere from the Coordinated Ocean-Ice Reference Experiments (CORE) (W. G. Large & Yeager, 2004; Griffies et al., 2009), with a 6-hour coupling frequency between the ocean, sea ice, and atmosphere for CESM-HR, and 24-hour for CESM-LR. Surface fluxes depend on the atmospheric and oceanic state and are calculated using the algorithms of W. Large and Yeager (2009). The effects of eddy-generated surface currents on surface wind stress (Martin & Richards, 2001) are incorporated in the forcing. In both configurations, the physical model was initialized using temperature and salinity fields from the World Ocean Circulation Experiment (Gouretski & Koltermann, 2004) and spun up for 15 years with CORE-forcing. The spin up is completed separately for CESM-HR and CESM-LR to enable kinetic energy to reach a stage of quasi-equilibration for each model configuration. Ocean biogeochemistry was initialized from available observationally-based World Ocean Atlas (WOA) climatologies (e.g. for O_2 and Nitrate) (Garcia et al., 2005) and, when not available, a CORE-forced hindcast simulation of CESM (Long et al., 2013), and spun up for one year in both model configurations to allow for ecosystem stabilization and development of mesoscale features in the tracer fields (Harrison et al., 2018). Both model configurations were integrated following this initialization using the CORE forcing for 5 years with outputs saved at a 5-day mean frequency. Under this short spin up, the simulated mesoscale field operates on large-scale biogeochemical tracer distributions that closely resemble the observations used as initial conditions. The repeating annual cycle used in the atmospheric forcing is well suited to addressing questions about the seasonal cycle and mean state dynamics in the absence of obfuscating inter-annual variability.

2.2 Particle Tracking & Vortex Identification

To examine the mechanisms by which TIVs influence oxygen transport, we conducted offline virtual particle tracking simulations and analysis of the CESM-HR 3D velocity field using Parcels (Van Sebille et al., 2018a), a grid-flexible and computationally-scalable Lagrangian simulator (Delandmeter & Van Sebille, 2019). Particle trajectories are computed using a fourth-order Runge–Kutta scheme for time-stepping the advection equation (Van Sebille et al., 2018b):

$$X(t + \Delta t) = X(t) + \int_{t}^{t+\Delta t} v(x(\tau), \tau) d\tau \tag{1}$$

where X(t) represent particle position, and $v(x(\tau), \tau)$ is the 3D Eulerian 5 day mean velocity field, linearly interpolated and integrated at a one day time-step (Δt). The effects of the linear interpolation of the 5-day mean velocity field were tested by coupling Parcels to a shorter 2 months physics-only simulation of CESM-HR with daily and 5 day mean velocities outputs, and differences in particle trajectories were found to be negligible.

Particle trajectories are computed forward in time to explore the fate and transport pathways of particles entrained by TIVs. We focus on a well developed vortex from the last year (year 5) of the simulation as a case study for clarity, noting generally similar processes at play across vortices and years. Particles are initially seeded at grid resolution (every 0.1°) and spaced at 10 m vertical intervals throughout the upper 300 m of the vortex. Particle trajectories are integrated forward for 90 days and their positions are sampled at each time step. These trajectories are examined to illustrate the eddy processes driving TIV associated lateral and vertical advection and water mass exchanges in the upper ocean, focusing on eddy trapping, stirring, and subduction effects.

Particle trajectories are also computed backward in time to evaluate their origin prior to their entrainment in the vortex cores. We seed particles using the same initialization set up for the forward runs, but run backward in time for 90 days. Particle properties are sampled at each time step, including longitude, latitude, depth, temperature, oxygen concentration, and density, allowing the evaluation of their source waters, depths, and trajectories prior to their final position in the eddy core. Several methods have been proposed to identify and track eddy structures in the open ocean. We identify TIVs using sea surface height (SSH) anomalies as well as the Okubo Weiss (OW) parameter (Okubo, 1970; Weiss, 1991), calculated as:

$$OW = (\frac{\partial u}{\partial x} - \frac{\partial v}{\partial y})^2 + (\frac{\partial v}{\partial x} + \frac{\partial u}{\partial y})^2 - (\frac{\partial v}{\partial x} - \frac{\partial u}{\partial y})^2 \qquad (2)$$

where u and v represents the surface zonal and meridional velocities respectively, and where $(\frac{\partial v}{\partial x} - \frac{\partial u}{\partial y})^2$ and $(\frac{\partial u}{\partial x} - \frac{\partial v}{\partial y})^2 + (\frac{\partial v}{\partial x} + \frac{\partial u}{\partial y})^2$ represent the relative rotational vs. straining components of the horizontal TIV flow, respectively (Dutrieux et al., 2008).

3 Model Validation:

We first evaluate the model simulation of equatorial Pacific circulation and O_2 distributions. Figure 1 compares the climatological annual and monthly mean surface velocities and their meridional shear in CESM-LR and CESM-HR to the NOAA Global Drifter Program product (Laurindo et al., 2017). In both configurations, CESM simulates relatively well the structure and location of the westward flowing SEC and NEC, and eastward flowing NECC (Fig 1a-c), though the magnitude of the NECC is noticeably weaker in both simulations, likely due to deficiencies in the wind forcing as also found in a recent eddy resolving simulation of CESM (Deppenmeier et al., 2021). We also note stronger shear along the equator in CESM-LR compared to CESM-HR associated with more defined north and south SEC branches at the lower resolution. The climatological seasonal cycle in zonal velocity (contours in Fig 1d-f) and its meridional shear (color shading) averaged over the TIV region show strong seasonality in the observations and models, with a more pronounced seasonal cycle in the model simulations of the SEC and NECC and their shear. This stronger seasonality is driven in part by the fact that zonal velocity and its shear during spring are substantially reduced in CESM-HR and CESM-LR as compared to the drifters. We do not expect these differences to have a major influence on TIV impacts, since TIVs are generated in both observations and models from mid-summer through mid-winter when the shear is strong enough for generating instabilities.

At depth, CESM-HR showcases a generally improved representation of the equatorial current system as observed by acoustic Doppler current profiler measurements (Johnson et al., 2002), including the location, magnitude, and structures of the SEC, NEC, and NECC (Fig 2d-f). The simulated OMZs structure and intensity are also improved at the 0.1° resolution (Fig 2b), which showcases a north tropical Pacific (NTP) OMZ extending further west and a more oxygenated EOT than the 1° resolution (Fig 2a), in general agreement with the CSIRO 2009 Atlas of Regional Seas (CARS) climatological O_2 estimates shown in Fig 2c (Ridgway et al., 2002). We also note a more intense and less tilted EUC in CESM-HR and the emergence of the NSCC and SSCC or "Tsuchiya jets" at this finer resolution, which may explain its deeper, broader, and more pronounced EOT

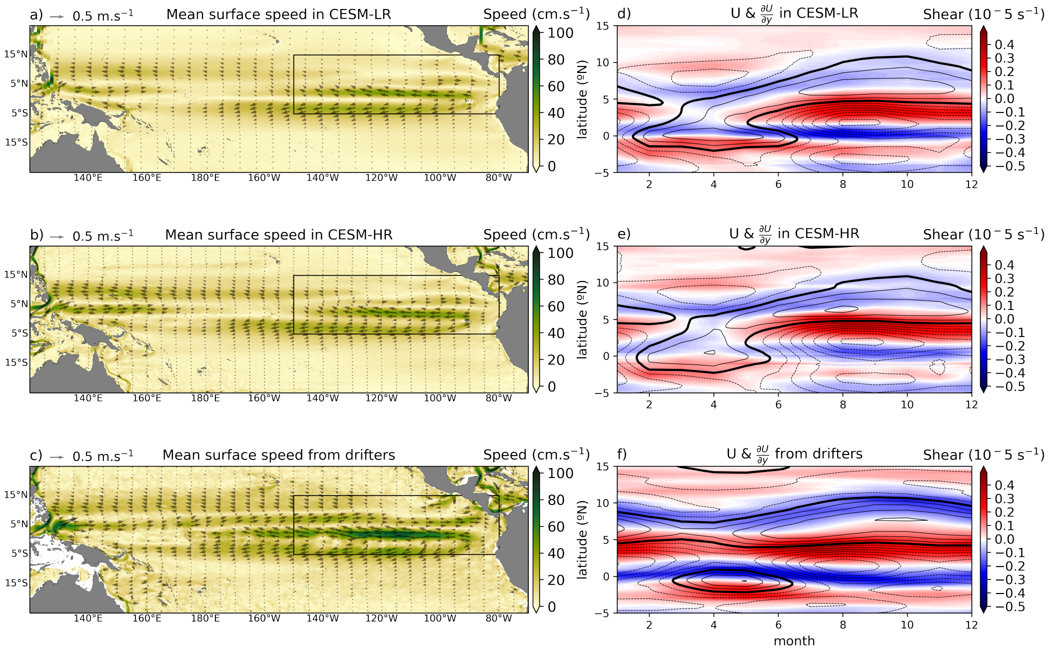

Figure 1. Climatological annual mean surface velocities (Left panels) in CESM-LR (a), CESM-HR (b), and NOAA drifter program estimates (Laurindo et al., 2017) (c). Right panels show monthly mean zonal velocity and its meridional shear (color shading) averaged over the 80°W-150°W region from d) CESM-LR, e) CESM-HR, and f) NOAA drifter program estimates (Laurindo et al., 2017). Monthly mean velocities are contoured every 0.1 m.s^{-1}. Negative values (i.e. easterly flow) are denoted by dashed lines. Solid thick line denotes the 0 m.s^{-1} contour. A depth of 15 m in both models is used here to represent the surface for consistency with the drifters.

(Fig 2d-i). These generally improved representation of subsurface jets and large scale O_2 distributions in CESM-HR are in line with recent eddy-resolving model studies that suggest a critical role for the EUC and other equatorial zonal jets in simulating the structure and intensity of the tropical OMZs (Duteil et al., 2014; Busecke et al., 2019).

Figure 3 shows snapshots of typical TIVs in CESM-LR and CESM-HR. The CESM-HR vortex is well defined by a cresting wave-like pattern of cold SST and intense anticyclonic circulation, with rotational velocities of order 1 m s^{-1} (Fig 3e) and strongly negative relative vorticity ($\zeta = \frac{\partial v}{\partial x} - \frac{\partial u}{\partial y}$) at the surface (Fig 3h). Strong poleward convergence of surface waters is evident along the leading edge, and induces intense downwelling velocities of about 20 m day^{-1} (Fig 3e-g). This poleward convergence and downwelling flow are balanced by divergence and broader equatorward upwelling along the trailing edge (Fig 3f-g). In contrast, the CESM-LR vortex exhibits much weaker lateral and vertical velocities, and a poorly defined vorticity structure (Fig 3a-d). The TIV features simulated by CESM-HR are in general agreement with the vortex structures reported in observations (Flament et al., 1996; Kennan & Flament, 2000) and finer model simulations of the Regional Ocean Model System (ROMS) at 4 km resolution (Marchesiello et al., 2011; Holmes et al., 2014), though more intense vertical velocities and complex submesoscale features emerge at these finer scales. Though in-situ observations are too sparse to fully validate the biogeochemical TIV response in the equatorial Pacific, CESM-HR simulates relatively well the cusp-like TIV-related features in surface chlorophyll (Supplementary Figure 1) previously reported in satellite observations (Strutton et al., 2001).

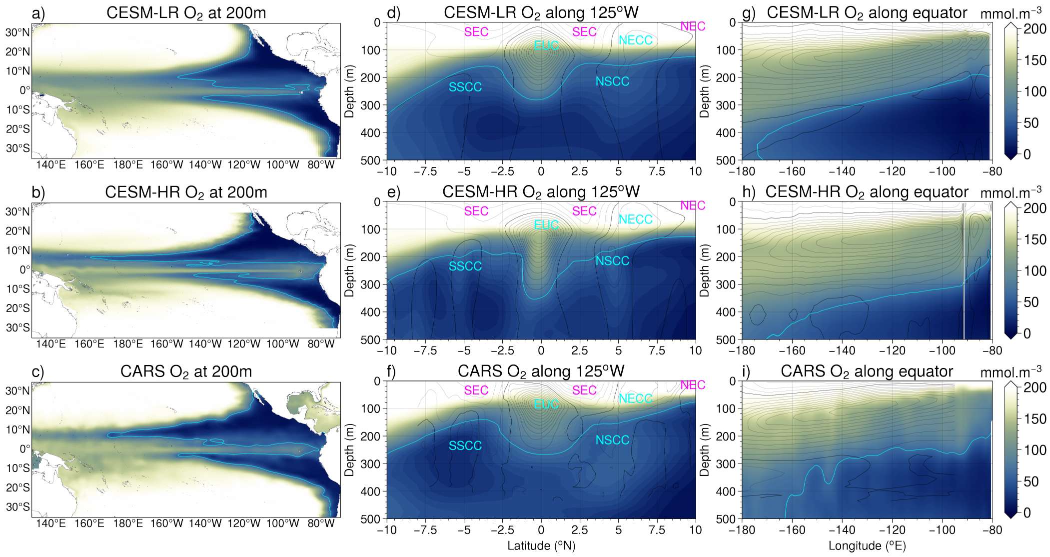

Figure 2. Climatological mean O_2 along the a-c) 200 m depth, d-f) the 125°W meridional section, and g-i) the equator, in CESM-LR, CESM-HR, and CARS. Cyan lines contours denote hypoxic (60 mmol.m^{-3}) contours. Climatological zonal velocity are superimposed in black line contours in d-f) and g-i) which denote zonal currents from CESM-LR, CESM-HR, and observations (Johnson et al., 2002), contoured every 0.1 m.s^{-1}, with solid line indicating the 0 m.s^{-1} contour. The direction of the main equatorial currents is shown in d-f) by the text color, with cyan colored currents (EUC, NECC, NSCC, and SSCC) flowing eastward, and magenta colored currents (SEC and NEC) flowing westward.

CESM-HR, with its improved representation of equatorial mesoscale circulation and O_2 distributions (Fig 1-3), thus presents a well suited ocean modeling tool to explore the influence of TIVs on the equatorial Pacific O_2 balance.

4 TIV Imprints on Equatorial Pacific Oxygen

The impacts of TIVs on O_2 distribution in the upper equatorial Pacific are illustrated in Figure 4. A series of vortices from a 5-day mean snapshot of October 3, year 5 of the simulation, is outlined at the surface by undulating cusp-like fronts in SST, strong anticyclonic surface circulation, and sea surface height anomalies of about 10 cm (Fig 4a-b). Figure 4c outlines the imprints of TIVs on O_2 at 155 m depth as highly oxygenated anomalies of order 50-100 mmol m^{-3} from about 2°N-8°N. These oxygenated features occur amidst largely hypoxic conditions at this depth and latitudinal range. TIV impacts on O_2 are initiated during vortex genesis in the eastern equatorial Pacific from about 100°W to 120°W, and are amplified as TIVs mature and propagate westward until about 160°W, where vortex demise weakens their impacts. No major eddy-related O_2 anomalies are noted south of the equator (Fig 4c), where the background O_2 content is less deficient due to more vigorous O_2 supply by the mean circulation and where eddy kinetic energy (EKE) is weaker and lacks coherent structure (Ubelmann & Fu, 2011).

The influence of the TIVs passage on temperature and O_2 at depth is illustrated in Figure 5, which shows a close up view along with zonal and meridional sections transecting the center of a fully developed vortex, named V3 hereafter (black box in Fig 4a). Strong TIV displacement of the isotherms from the surface to 500 m depth is evident

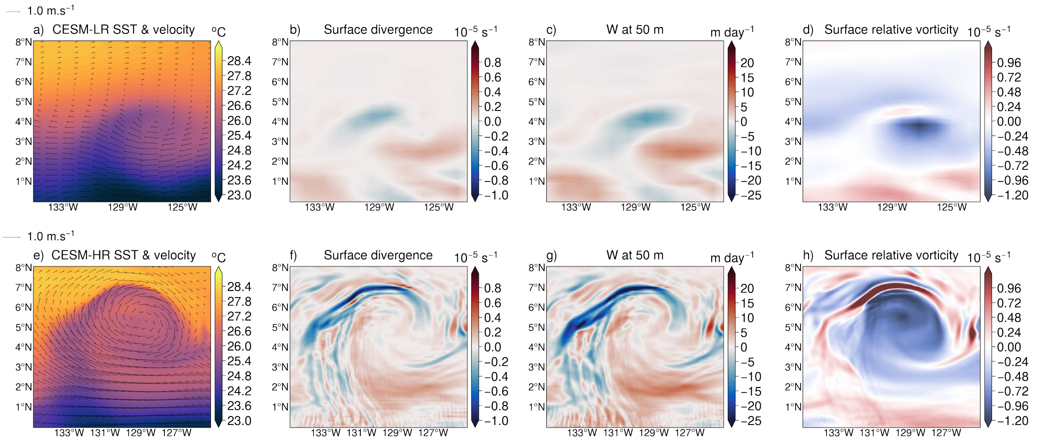

Figure 3. Snapshot of simulated sea surface temperature (SST) and surface velocity, surface divergence, vertical velocity at 50 m depth, and surface relative vorticity ($\zeta = \frac{\partial v}{\partial x} - \frac{\partial u}{\partial y}$) in CESM-LR (a-d) and CESM-HR (e-h). Positive vertical velocity in c) denotes upwelling, while negative values represent downwelling. Positive values in b) denote surface divergence while negative values indicate surface convergence. The 5-day mean snapshots used for CESM-LR and CESM-HR are for September 28, year 5 and October 3, year 5, respectively.

(Fig 5c and 5e), inducing a lens shaped isopycnal disturbance in the upper thermocline. The vortex depression of the thermocline is accompanied by a deepening of the northern equatorial Pacific hypoxic boundary by 50-100 m from 2°N-8°N and an expansion of the equatorial oxygenated tongue (cyan line in Fig 5d and 5f). A bolus of strongly oxygenated water occupies the eddy core, outlined in Figure 5d and 5f by the σ_θ=22.7-24.5 isopycnal range (grey thick lines), and exhibits complex O_2 features that are distinct from the isopycnal and temperature structures imposed by the vortex flow (Fig 5c and 5e). Maxima in O_2 anomalies surround the eddy center in the 100 m depth range (e.g. along 127°W and 132°W in Fig 5d and 5f) and are superimposed on colder isotherms (and thus denser isopycnals). An upward heave of isopycnals should lead to less O_2, instead the heaving isopycnals along 132°W and 127°W shown in Figure 5c and along 7°N in Figure 5e are associated with higher O_2 concentrations (Figure 5d and 5f), suggesting strong advective or diapycnal mixing processes may be driving the TIV oxygenation in this depth range.

Figure 6 showcases the subsurface O_2 imprints of the TIVs shown in Figure 4 on density surfaces. Positive TIV related O_2 anomalies are found on isopycnals from the outcropping layers down to the base of the vortex cores (σ_θ=24.5), and tend to follow the TIV cold SST front (Fig 6a-b). Poleward and downward velocities of about 0.5-1 m.s^{-1} and 15-20 m.d^{-1} , respectively, emerge along the leading edge of the TIVs and are balanced by equatorward return flow along the trailing edge (Fig 6e-f). The structure and magnitude of the TIV flow and its associated oxygenation generally peak near 120°W-140°W and gradually wane as TIVs translate west. The vortex O_2 and velocity structures are most pronounced above the σ_θ=24.5 isopycnal, though TIV-related changes in oxygen and meridional and vertical velocities can be found down to the σ_θ=26.0 isopycnal (Fig 6d-f). The vortex oxygenation of the upper equatorial Pacific shown in Figure 4-6 thus defies a simple explanation by isopycnal displacement alone, and suggests an important role for O_2 transport by TIVs in influencing the structure of northern upper equatorial Pacific O_2 and OMZ variability on seasonal timescales and beyond.

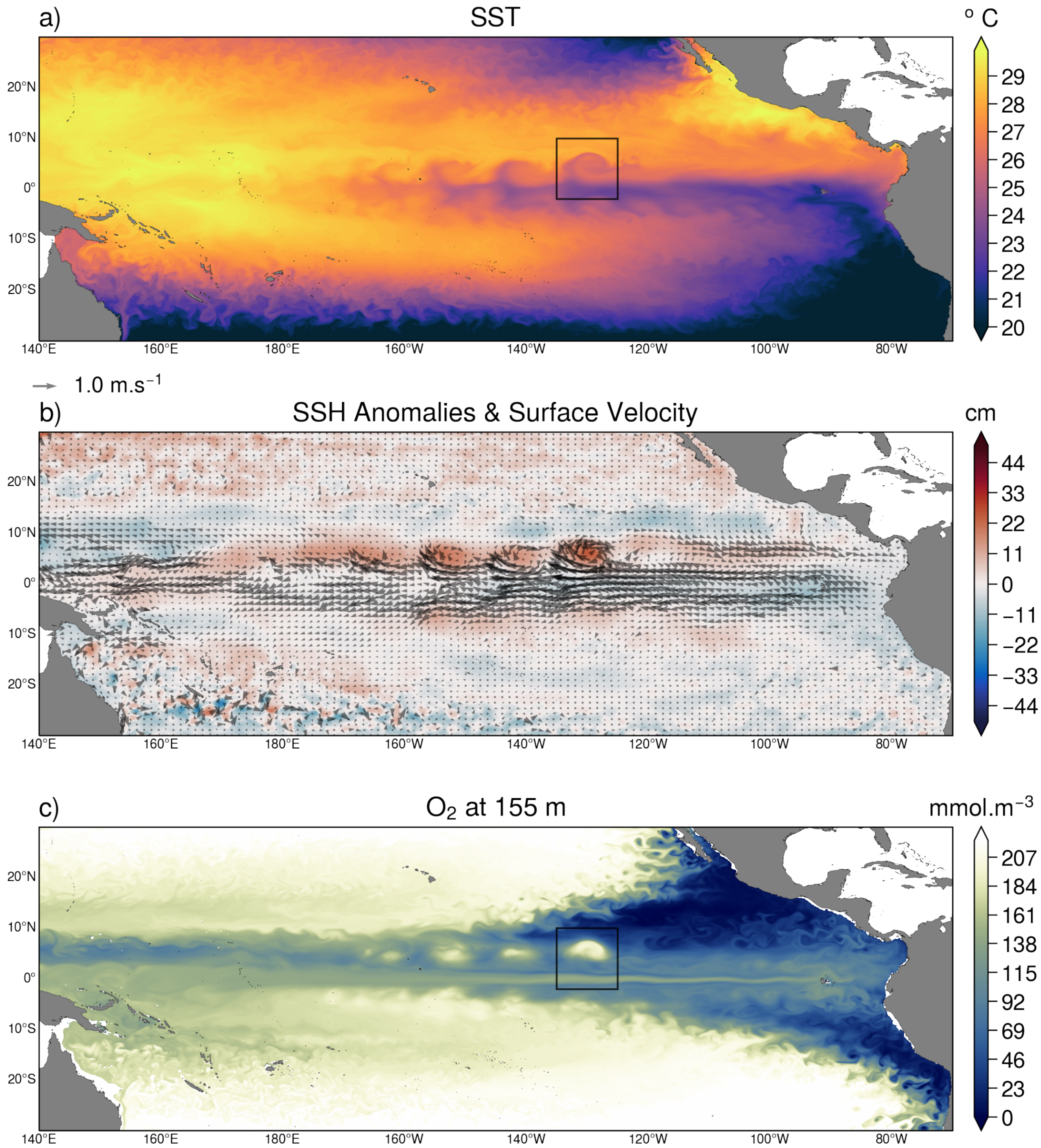

Figure 4. a) SST, b) sea surface height (SSH) anomalies and surface velocity, and c) O_2 at 155 m depth from a 5-day mean snapshot of October 3, year 5 of the CESM-HR simulation. The passage of TIVs is outlined by cusps of cold SSTs and anomalies in SSH of about 10 cm.

5 Seasonal Modulation

The generation of TIVs and their propagation along the northern equatorial Pacific exhibit strong seasonality, with vortices typically developing in summer, intensifying in fall, and subsiding by winter (Legeckis, 1977; Zheng et al., 2016; Willett et al., 2006). This seasonality is thought to be driven by the annual cycle of the prevailing cross-equatorial southerly winds, which modulates Ekman downwelling north of the equator and drives westward propagating Rossby waves, giving rise to a SSH ridge along 5°N (Wang et al., 2019). This seasonal modulation of the shear between the zonal currents in the eastern equatorial Pacific leads to the development of barotropic and baroclinic instabilities that generate strong EKE from boreal summer through winter (Willett et al., 2006; Wang et al., 2019). This seasonality in the zonal velocity shear and EKE is relatively well repro-

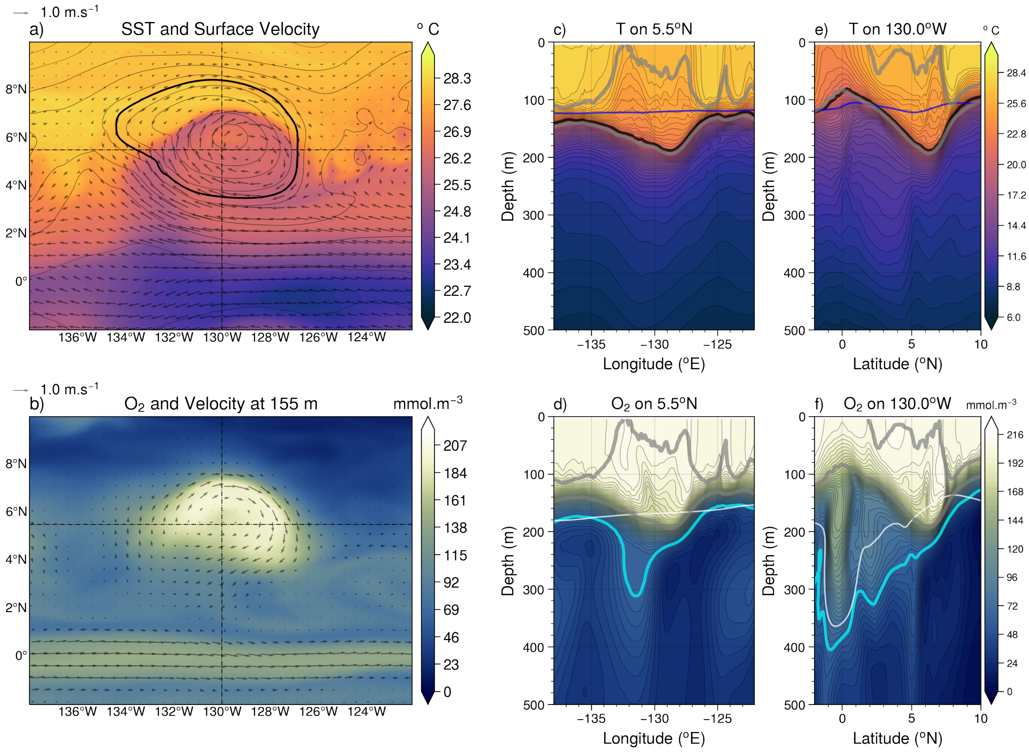

Figure 5. Close up view of vortex 3 (V3) outlined by the black square in Figure 4a from a 5-day mean snapshot of October 3, year 5 of CESM-HR. Panel a) shows SST, surface velocity, and SSH anomalies contoured every 4 cm, with the 10 cm SSH anomaly shown in bold. Panel b) shows O_2 and velocity at 155 m depth. c) and d) show zonal (east-west) sections of temperature and O_2 along 5.5^{o}N. e) and f) show meridional (north-south) sections of temperature and O_2 along 130^{o}W. Grey bold lines in c-f) outline the σ_θ=22.7 and σ_θ=24.5 isopycnal surfaces bounding the vortex core, while the solid black and blue lines outline the 21°C isotherm for the 5 day mean snapshot and climatological mean respectively. The cyan and white contours in d) and f) outline hypoxic values (O_2 = 60 mmol.m^{-3}) for the 5-day mean snapshot and climatological mean, respectively. The depth sections longitude (130^{o}W) and latitude (5.5^{o}N) are outlined in dashed black lines in panels a) and b) for reference.

duced in CESM-HR, which showcases a maxima in the meridional shear in surface zonal velocity along 5°N during August-September (Fig 1e), driving stronger EKE and higher frequency of TIVs from mid-summer through mid-winter (Fig 7h).

The seasonal cycle of TIV activity is approximately in phase with the seasonal cycle of the simulated OMZ structure and O_2 content of the upper northern equatorial Pacific. Figure 7a-d shows the seasonal climatological mean O_2 at 155 m depth for winter, spring, summer, and fall. Strong oxygenation of the upper northern equatorial Pacific is especially evident during fall in the TIV region at 155 m depth (Fig 7d) and throughout the upper 250 m (not shown), while spring exhibits much lower O_2 at these depths (Fig 7b). Figure 7a-d and 7e further highlight the effects of this seasonal oxygenation on the westward extent of the NTP OMZs at 155 m depth, whereby the hypoxic boundary along 6°N shoals westward to about 160°W during boreal spring and recedes back to about 120°W during peak TIV season (fall). An expanded view of year 5 of the CESM simulation (Fig 7f-g) highlights the passage of TIVs as major oxygenation events that

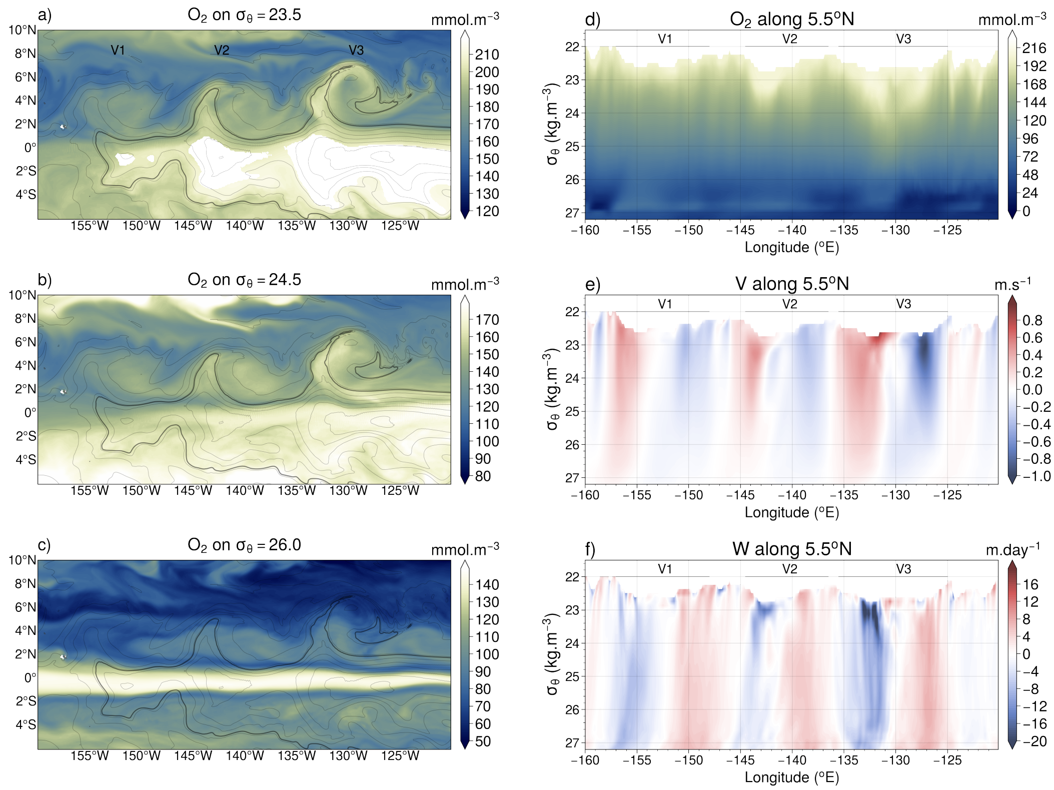

Figure 6. O_2 on the a) 23.5, b) 24.5, and c) 26.0 potential density surfaces (σ_θ) from a 5-day mean snapshot of October 3 of year 5 of the CESM-HR simulation. d), e) and f) show longitudinal sections of O_2, and meridional and vertical velocities on density coordinates along 5.5°N, respectively. Positive (red) meridional and vertical velocities denote northward and upward flow, respectively. Grey thin lines in a)-c) outline SST, contoured every 0.5°C, with the 26.0°C isotherm contoured in bold. The three most prominent vortices shown in Figure 4 are outlined as V1, V2, and V3.

modulate the vertical extent of the NTP OMZ westward extension: the oxygen concentration at 155 m varies by 50-100 mmol m^{-3} and the hypoxic depth varies by 50-100 m as the TIVs propagate past over about a month's time (Fig 7g). The seasonal O_2 imprints of TIVs on density coordinates in CESM-HR are also identified for the full simulation (Supplementary Figure 2a) as highly oxygenated features that penetrate down to the σ_θ=26.0 density layer from late summer through early winter. Most notably, the TIV modulation coincides with peak seasonal oxygen concentrations at 155 m and the deepest hypoxic depth during boreal fall (Fig 7f-g); thus TIVs are crucial to the genesis of the most deeply penetrating oxygenation events during the entire annual cycle.

The simulated mean seasonal cycle of the O_2 content integrated over the upper ocean (0-200m) in the TIV region (black box in Fig 7a-d) is shown in Fig 7h, oscillating from a maxima of about 96 Tmol during peak TIV season (September/October/November), to a minima of about 81 Tmol when TIVs are largely inactive (April/May/June). The seasonality of ecosystem habitable and vertical foraging space in this region is strongly tied to the variability of the hypoxic volume, which expands and contracts with the arrival of TIVs over the upper 200 m of the TIV region by about 50% with respect to the mean (Fig 7i). The seasonality in the O_2 content in the TIV region is also evident when integrated over the 23.5-26.0 density range (Supplementary Figure 2b), which shows a

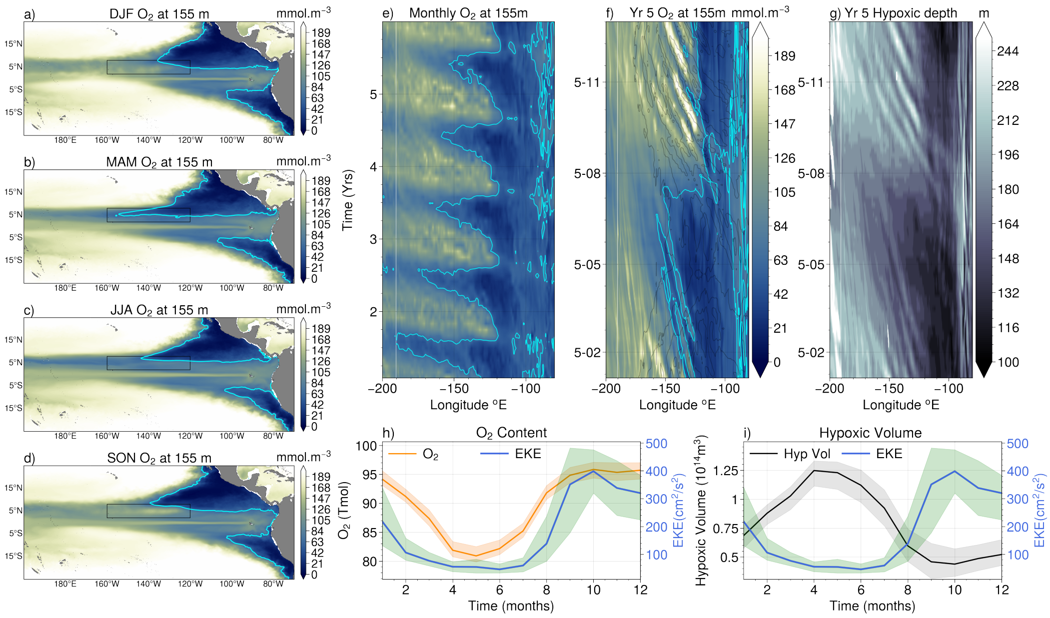

Figure 7. Seasonal climatological mean O_2 at 155 m depth in CESM-HR during boreal a) winter, b) spring, c) summer, and d) fall. The cyan line denotes the hypoxic boundary. Panel e) shows time-longitude diagram of O_2 along 6°N at 155 m depth using monthly averaged outputs for the full 5 year simulation of CESM-HR. The last year of this simulation at 5 daily-mean output frequencies is shown in f) along with hypoxic depth in g). Black contours in f) indicate SST along 2°N contoured every 1°C. Panels h) and i) show the climatological monthly means of the O_2 content and hypoxic volume integrated over the TIV propagation region bound by 120°W-160°W, 2°N-8°N, 0-200m depth range, along with EKE (blue) near the surface (15m depth) averaged over the same area shown in a black box in panels a-d. EKE ($\frac{U'^2+V'^2}{2}$) is calculated using anomalies from the 3-months running mean of the velocity field at 15 m depth. Shading in h-i) bounds the minimum and maximum monthly mean values over the 5 year simulation. Seasonal climatologies shown in a-d) are averaged over the monthly means of December, January, and February (DJF) for winter, March, April, and May (MAM) for spring, June, July, and August (JJA) for summer, and September, October, and November (SON) for fall.

tight relationship to EKE in this region. Various processes may also contribute to the seasonal variability in the northern upper equatorial Pacific O_2 content and habitable space, including seasonal changes in the supply of O_2 by the tropical and subtropical cells and equatorial zonal jets, basin scale adjustment of the isopycnals to wind forcing, and seasonality in the vertical mixing of O_2. Isolating the contribution of these different processes on the equatorial Pacific O_2 budget balance and their interactions with TIV processes and their potential rectified effect on the seasonal cycle merit closer investigation but is outside the scope of this work, which aims at assessing the local impacts and mechanisms of mesoscale eddies on O_2 distributions.

6 Mechanisms of Vortex Oxygenation

Throughout their westward propagation, TIVs advect and mix waters laterally and vertically (Kennan & Flament, 2000; Dutrieux et al., 2008; Holmes & Thomas, 2015; Cherian et al., 2021), redistributing nutrients and carbon, and modulating primary productivity (Menkes et al., 2002; Strutton et al., 2001, 2011; Gorgues et al., 2005). The simulated seasonal vortex oxygenation of the northern equatorial Pacific in CESM-HR thus likely reflects the influence of both physical and biogeochemical processes, including TIV-mediated changes in advection, turbulent mixing, air-sea gas exchange, photosynthetic production, and microbial consumption of sinking detritus. In this section, we explore the contribution of these processes to the TIV modulation of the upper equatorial Pacific O_2 budget balance in CESM-HR and examine the eddy processes governing TIV advection using Lagrangian particle tracking simulations.

6.1 TIV Modulation of the O_2 Budget:

We evaluate the contributions of physical and biogeochemical processes to the O_2 balance, calculated as follows:

$$\frac{\partial O_2}{\partial t} = -\nabla \cdot (\mathbf{u}O_2) + D(O_2) + \frac{\partial}{\partial z} k \cdot \frac{\partial O_2}{\partial z} + J(O_2) \tag{3}$$

where $-\nabla\cdot(\mathbf{u}O_2)$ represents the effects of zonal, meridional and vertical advection, $D(O_2)$ and $\frac{\partial}{\partial z}k\cdot\frac{\partial O_2}{\partial z}$ represent lateral and vertical diffusive mixing contributions (including KPP), respectively, and $J(O_2) = Prod(O_2) - Cons(O_2)$ represents the net balance of sources (plankton photosynthetic production) and sinks (microbial consumption) of O_2.

Figure 8 summarizes the contribution of these different terms to the upper equatorial Pacific O_2 budget, integrated over the 100-200m depth range which contains the oxycline and hypoxic boundary, and showcases the largest TIV-induced O_2 changes (Fig 4 and 5). The arrival of TIVs during late summer and fall in a box bound by 3°N-7°N, 127°W-133°W, and 100-200m depth (green box in Figure 8e), is marked by strong fluctuations in the values of the Okubo-Weiss parameter and pronounced increases in the O_2 content (Fig 8a-d). The TIV-induced changes in the O_2 content are driven largely by advective effects which are dominated by vertical advective redistribution of O_2 from the overlying upper 100 m (Fig 8b-d) associated with lateral convergence in this depth range.

Figure 8e-k outlines the spatial characteristics of the contribution of these different budget terms to the TIV-induced O_2 changes integrated over the 100-200 m depth range. The advective terms drive a substantial O_2 increase along the western edge of the vortices (outlined by SST contours) and a decrease along their eastern edges, with the vertical advective term driving a net influx of oxygen to the 100-200m depth range along contours of intense TIV downwelling (Fig 8j). The contribution of the vertical advective term may reflect both the effects of eddy pumping by the vortex anticyclonic flow as well as the subduction of surface waters along sloping isopycnals by the intense downwelling along the vortex cold front (Fig 3g and Fig 6). Smaller but mainly positive contributions from vertical diffusive mixing are concentrated near the equator (Fig 8g). The effects of microbial respiration are much smaller relative to the advective and mixing effects, and act mainly to reduce O_2, though only slightly, in the vortex core (Fig 8k). The contribution of lateral diffusive mixing is negligible and is not shown here for brevity.

Though the instantaneous effect of vertical mixing is relatively small compared to the advective terms, it sustains a net positive flux of oxygen from the mixed layer to the thermocline (Fig 8d and 8g). Vertical mixing flux of O_2 is intensified at the base of the mixed layer along the 2°S-2°N band of the leading edge of the TIVs. This mixing is superimposed on patches of positive surface Apparent Oxygen Utilization (AOU) values and enhanced air-to-sea flux of O_2 (Fig 8h and 8l), indicative of entrainment of low-O_2 thermocline waters to the surface and their subsequent exposure and equilibration with the atmosphere. Downward mixing of O_2 is also slightly elevated along TIV cold cusps up to about 6°N, consistent with enhanced mixing due to TIV shear north of the equator (Cherian et al., 2021). Analogous mixing effects on the equatorial heat balance have

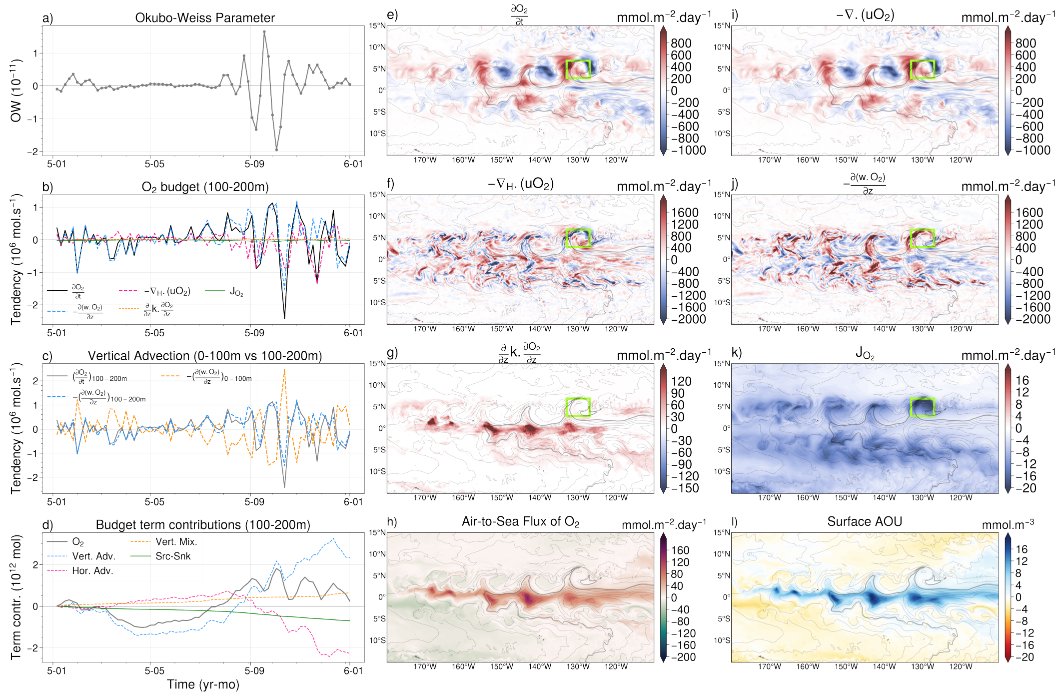

Figure 8. a) Okubo Weiss parameter, b) budget terms integrated over the 3°N-7°N, 127°W-133°W, 100-200 m range shown in green box in e) from January through December of year 5 of CESM-HR. Panel c) compares the O_2 tendency and vertical advective term integrated over the 100-200m to the vertical advective term integrated over the upper 0-100m. d) shows the contribution of the various budget terms in b) through their cumulative sum in time to the O_2 content anomaly integrated over the 100-200m depth range, using time=0 (Jan 1, year 5) as a reference. e-g) and i-k) show maps of the O_2 budget terms integrated over the 100-200m depth range in a 5-day mean snapshot of Oct 3, year 5 of CESM-HR. Note different color bar scales for the budget terms to highlight spatial patterns. Red denotes net positive flux of O_2 into the depth range. h) and l) show the air-sea flux of O_2 (positive to ocean) and Apparent Oxygen Utilization (AOU) at the surface for the same time snapshots. Grey thin lines in e)-l) outline SST, contoured every 0.5°C, with the 26.0°C isotherm contoured in bold. The effects of lateral diffusive mixing are negligible in CESM-HR and are not shown for brevity.

been widely reported in observations and modeling studies and have been associated with vortex modulation of the shear in zonal flow and stratification (Lien et al., 2008; Moum et al., 2009; Holmes & Thomas, 2015; Inoue et al., 2019; Cherian et al., 2021).

A key question of interest concerns the extent to which direct physical O_2 supply by advective and mixing processes is compensated by TIVs indirect influence on respiration rates through changes in nutrient delivery, primary productivity and carbon export. Previous work has shown that TIVs induce major changes in the biogeochemical and ecological structures and dynamics of the equatorial oceans (Menkes et al., 2002; Strutton et al., 2001, 2011; Gorgues et al., 2005; Evans et al., 2009). In CESM-HR, TIVs are associated with enhanced phytoplankton mass (chlorophyll and carbon) along their cold cusp (Supplementary Figure 3). This is driven primarily by diatoms and small phytoplankton, which in turn lead to enhanced zooplankton grazing and intensified particulate organic carbon (POC) production in the upper ocean (Supplementary Figure 3). The consumption of O_2 in TIV cores increases by about 4-fold in CESM-HR (Fig 8k), driven by enhanced microbial respiration and remineralization of TIV advected and newly produced POC. The contribution of TIV-enhanced microbial respiration to the O_2 balance, however, is more than an order magnitude smaller than the advective and mixing terms (Fig 8e-k), suggesting negligible compensation by TIV biogeochemical effects. These simulated eddy effects stand in contrast to the observed large O_2 depletion rates found in ACMEs in the EBUS regions (Karstensen et al., 2017; Schütte et al., 2016), though biogeochemical observations of TIVs are needed to allow for a more adequate comparison.

6.2 Pathways of TIV Advection:

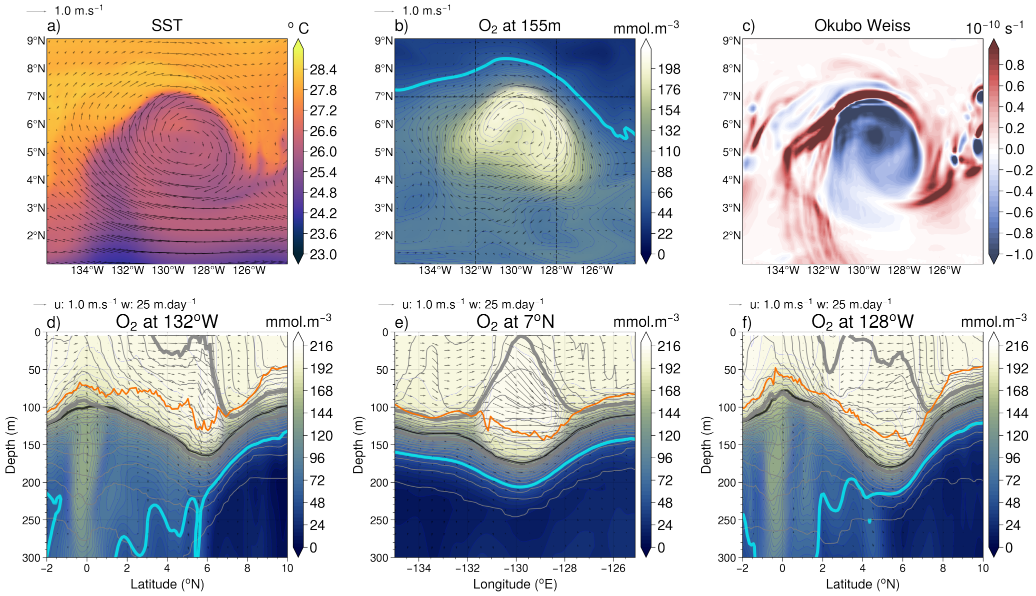

Figure 9. A close up view of V3 from a 5 day mean snapshot of Oct 3 year 5 of a) SST and surface velocities, b) O_2 and lateral velocities at 155 m depth, and c) surface Okubo Weiss parameter. Bottom panels show a 3D view of O_2 distribution and velocity in V3 along d) 132°W, e) 7°N, and f) 128°W, outlined in dashed black lines in panel b). The solid black and orange lines in d-f) outlines the 21°C isotherm and mixed layer depth (defined using a maximum buoyancy gradient criteria), respectively, while the cyan line denotes hypoxic contours. Grey bold lines indicates the σ_θ=22.7 and σ_θ=24.5 isopycnals bounding the vortex core. Grey thin lines in d)-f) outline σ_θ at 0.2 intervals.

The dominance of TIV advective effects on the O_2 balance in the climatological thermocline and oxycline depth range shown in Figure 8 reflects complex and intense redistribution of O_2 in the upper equatorial Pacific by the vortex flow. These include i) isopycnal displacement by eddy pumping, ii) zonal advection and westward translation by eddy trapping, iii) latitudinal advection and mixing through eddy stirring of meridional gradients, and iv) the along-isopycnal transfer and exchange of waters from the oxygenated surface to the base of the mixed layer and upper thermocline through subduction and upwelling associated with frontogenesis. For clarity, we examine these eddy advective processes by analyzing particle trajectories seeded in a single TIV (V3 detailed in Fig 9 and Fig 5) as a case study. We note largely similar structures, particle trajectories, and mechanisms emerging across the simulated TIVs of CESM-HR.

i) Eddy Pumping: Similar to anticylonic mode water eddies, TIV flow induces a lens-shaped disturbance in the isopycnal structure of the upper thermocline (Fig 5c-f and Fig 9d-f). Eddy pumping by the eddy anticyclonic flow depresses isopycnals in the main thermocline, explaining much of the deepening of the hypoxic depth. Figure 10c shows the evolution of particles seeded in V3, whereby particles seeded below the σ_θ=24.5 isopycnal surface, which closely outlines the 21°C isotherm, respond to the TIVs passage largely through vertical displacement associated with the vertical movement of the isopycnals. Above the 21°C isotherm, however, the O_2 structures induced by TIVs deviate significantly from what's expected from isopycnal displacement (Fig 9d-f), with some of the largest O_2 changes found along contours of vertical and lateral velocity maxima.

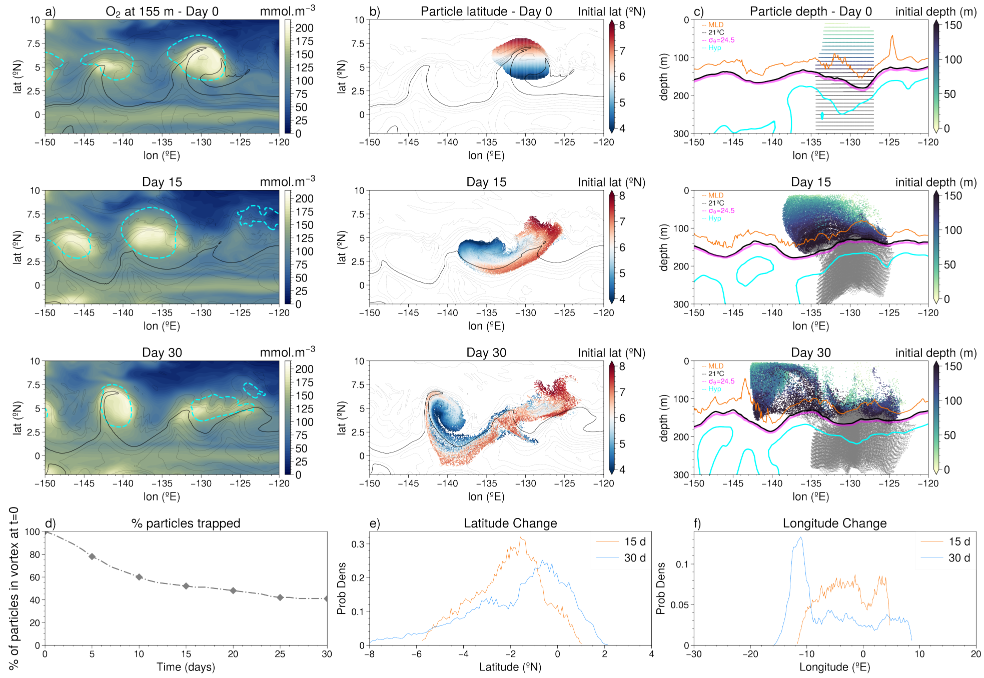

Figure 10. Forward Lagrangian simulations of particles seeded in the core of V3. a) O_2 at 155 m depth from the initial time step (Oct 3, year 5) through day 30. Cyan contours denote 10 cm SSH anomalies used to outline TIV core waters. b) Location of particles seeded in the core of V3, with initial particle latitude at time=0 shown in color. Grey thin lines in a) and b) outline SST, contoured every 0.5°C, with the 26.0°C isotherm contoured in bold. c) The depth vs longitude profiles of particles with initial particle depth in color shading, and contours of mixed layer depth (orange), 21°C isotherm (black), the σ_θ=24.5 isopycnal surface (magenta), and hypoxic boundary (cyan). Particles in grey are initialized below the σ_θ=24.5 isopycnal surface, while color shaded particles are initialized in the σ_θ=22.7-24.5 isopycnal range. d) Percent of particles remaining in the vortex core with time. e) and f) show PDFs of latitudinal and longitudinal change of particles after 15 and 30 days.

ii) Eddy Trapping: TIVs exhibit intense anticyclonic circulation in CESM-HR from the surface down to the base of the mixed layer with large rotational velocities (∼1 m/s) that exceed their translational speed (∼ 0.4 m/s). This anticyclonic flow is characterized by negative ζ and Okubo Weiss parameter values (Fig 9a-c) and Rossby numbers of $O(1)$; these characteristics are indicative of non-linear flow and strong trapping of water masses and their zonal advection by the TIV westward translation. Figure 10 illustrates this effect in particles seeded in the core of V3, where about 40% of the particles are advected about 10° west after 30 days through eddy trapping (Fig 10d and 10f). Similar eddy trapping effects were found in previous Lagrangian particle simulations of equatorial Pacific (Holmes et al., 2014) and Atlantic TIVs (Dutrieux et al., 2008), who found about 50% of particles typically remaining in the eddy core after a full rotation (approximately 30 days). Figure 10 thus suggests that a significant portion of the oxygenated waters transported by TIVs are advected westward from the eastern equatorial Pacific. We further note that this eddy trapping effect is confined to particles above the the 21°C isotherm (see colored vs gray particles trajectories in Fig 10c), reflecting a decoupling of the vortex flow below the main thermocline and no major TIV-induced zonal transport of O_2 at the OMZ depth.

iii) Eddy Stirring: TIVs showcase intense anticyclonic flow from the surface through the upper thermocline, defined here as the isopycnal range between the base of the mixed layer and the 21°C isotherm (Fig 9). The region of rotation-dominated vorticity (negative OW in Fig 9c) is surrounded by a band of strongly positive OW values, which reflect strain-dominated flow and enhanced dispersion and stirring along the vortex periphery. Figure 10b and 10d illustrates the effects of eddy lateral stirring, whereby 60% of particles initially seeded within the vortex core were shed throughout the eddy translation around its periphery, and experienced substantial lateral stirring and latitudinal shifts of 2° to 8°, also in general agreement with the trajectories of particles seeded in the Atlantic vortices (Dutrieux et al., 2008). TIVs dispersive effects thus act to blur the sharp latitudinal gradients of O_2 set by zonal advection and consumption of O_2 at depth.

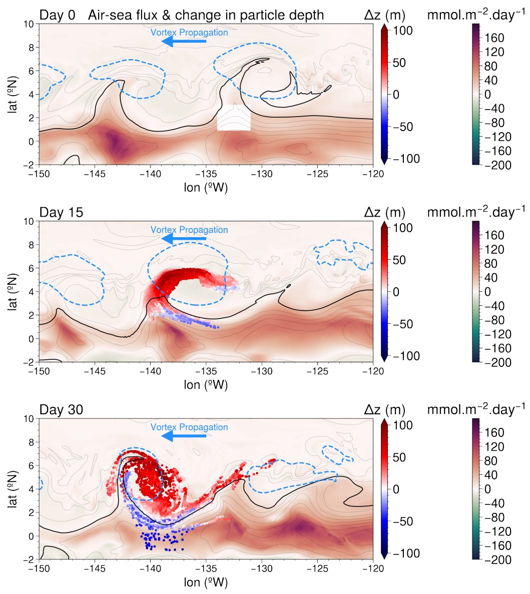

Figure 11. Air-sea flux of O_2 and locations and change in depth (Δz) of particles seeded in the upper 100 m of the southwest corner of V3 and run forward in time. Particle colors show change in depth since time=0. Grey thin lines outline SST, contoured every 0.5°C, with the 26.0°C isotherm contoured in bold, with dashed blue line denoting SSH anomalies of 10 cm outlining the TIVs. Particles are seeded throughout the upper 100 m from 5 m to 95 m depth at a vertical resolution of 10 m.

iv) Vortex Subduction and Upwelling: An important feature of TIV circulation is the convergence of surface waters along the SST cold front, which induces intense downwelling of order 20 m.day^{-1} (Fig 9d-e and Fig 3e-g) along the leading edge. The vortex core O_2 maxima are tightly associated with these vertical velocities, which arise from ageostrophic submesoscale circulation associated with frontogenesis (Marchesiello et al., 2011; Holmes et al., 2014). The downwelling of this oxygenated bolus is visible along the zonal section transecting 7°N (Fig 9e). Along with the dominance of the vertical advective term shown in Figure 8, we propose subduction, the along-isopycnal poleward transfer of water masses by convergence-induced downwelling along the leading edge of TIVs, as a major driver for the spiraling pattern of high O_2 shown at depth (Fig 9b). Observations and Lagrangian simulations of Pacific and Atlantic vortices (Kennan & Flament, 2000; Menkes et al., 2002) have reported similar intense downwelling velocities and identified the subduction of particles into the eddy core to occur mainly through its southwest corner (Dutrieux et al., 2008; Holmes et al., 2014). A similar downwelling pathway of oxygenated surface waters in CESM-HR can be visualized in Figure 11 by the trajectories of particles seeded in the upper 100 m of the southwest corner of V3, where intense air-sea flux and vertical diffusive mixing of O_2 occur (Fig 8). Nearly all particles initiated in the upper 100 m of the southwest corner of V3 are entrained into the eddy core and subduct along its leading edge, experiencing substantial depth increases (50-100m) within 15 days of entering the vortex. This subduction takes on a spiraling pathway along sloping isopycnals into the base of the mixed layer and upper thermocline, where some particle are dispersed along the vortex trail while others are upwelled back to the surface near the equator (Fig 11). This poleward subduction, equatorward upwelling, and shedding of newly oxygenated waters at the base of the mixed layer and upper thermocline occurs throughout TIVs propagation, suggesting vertical eddy advective fluxes may serve as an important pathway of O_2 supply from the surface to the ocean's interior.

The combined effects of these eddy advective processes help explain the source and formation mechanisms of the oxygenated vortex core waters. The backward Lagrangian simulation shown in Figure 12 traces the origin of oxygenated (O_2 > 180 mmol.m^{-3}) particles occupying the base of the eddy core (σ_θ=23.5-24.5 isopycnal range) which oxygenates the typically hypoxic depths during TIV translation. These particles originate further up the water column (Fig 12c and 12e), with two main peaks in the PDFs of their latitudinal and temperature of origin that are characteristic of EUC and NECC waters (Fig 12b, 12d, 12f, and 12h), as also noted in a previous Lagrangian simulation of equatorial Pacific TIVs (Holmes et al., 2014). Figure 12b shows that O_2 in these waters is about 40-60 mmol.m^{-3} less than its final concentration in the eddy core (day 0), with most of the O_2 increase occurring during their entrainment into the vortex near the EUC/SEC shear region (Fig 12d). In this region, intense air-sea flux and vertical mixing of O_2 takes place (Fig 8g-h) prior to the poleward subduction of particles (Fig 11).

The forward and backward particle trajectories examined in this study reveal numerous processes by which TIVs can advect O_2 in the upper equatorial Pacific, which we summarize in Figure 13. While eddy pumping explains much of the O_2 anomalies below the main thermocline, the effects of the 3D eddy circulation dominate in the upper ocean (above the 21°C isotherm). Eddy trapping, stirring, and subduction combine to drive an anticyclonic injection of surface waters and upper EUC and NECC waters to the base of the mixed layer and upper thermocline. These oxygenated waters are advected westward and shed along the vortex trail. This subduction is balanced by upwelling which entrains upper thermocline low-O_2 waters towards the equator, intensifying vertical mixing and uptake of O_2 at the surface. The subsequent spiraling injection of these surface oxygenated waters to the ocean's interior and upwelling of thermocline waters to the surface suggest that TIV play an important role in the replenishment of oxygen in the upper thermocline, with important implications for understanding the role of eddy transport in ventilating the upper equatorial OMZ and setting the depth of hypoxia and its seasonal variability.

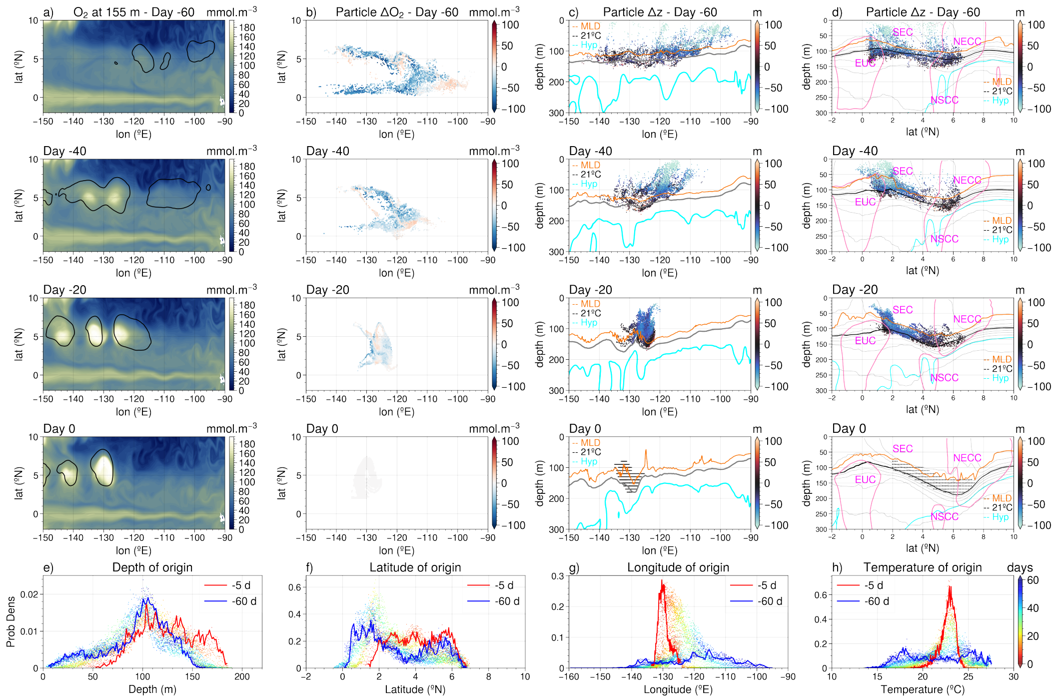

Figure 12. Backward Lagrangian simulation of particles seeded at the base of V3. a) O_2 at 155 m depth from 60 days prior (day -60), through day 0 (Oct 3 year 5) of the backward simulation with black contours denoting SSH anomalies of 10 cm outlining the TIVs location. b) Location of particles seeded in core of V3 with color shading indicating changes in O_2 from day 0. c) Depth vs longitude profile of particle location with color shading indicating changes in particle depth from day 0, along with mixed layer depth (orange), 21°C isotherm (black), and hypoxic boundary (cyan) along 5°N. d) Depth vs latitude profile of particle location with color shading indicating changes in particle depth from day 0, along with the location of the zonal equatorial currents (magenta), mixed layer depth (orange), 21°C isotherm (black), and hypoxic boundary (cyan) along 130°N. e-h) PDFs of particles depth, latitude, longitude, and temperature of origin are shown respectively, with colorbar indicating days before initiation (day=0).

7 Summary and Discussion

In this study, we examine the imprints of mesoscale eddies on the O_2 structure and variability of the upper equatorial Pacific using an eddy resolving simulation of CESM. We find that the seasonal generation and propagation of TIVs from boreal summer through winter lead to a substantial oxygenation of the northern upper equatorial Pacific, contributing to the seasonal shoaling and deepening of the westward extension of the northern tropical Pacific OMZ. This oxygenation is driven largely by transient TIV-induced isopycnal displacement at depth as well as the lateral and vertical advection of oxygen by the vortex flow. This is reinforced by TIV-enhanced vertical mixing and air-sea flux near the equator, and counterbalanced, though only slightly, by enhanced microbial respiration of oxygen in the eddy cores (see summary in Fig 13).

The relative contribution of these mechanisms and their interaction likely vary with the background O_2 gradient and depth of the vortex circulation as TIVs evolve from their genesis region in the O_2 depleted eastern equatorial Pacific to their destruction in the more oxygenated west. Dedicated observations and model simulations at finer tempo-

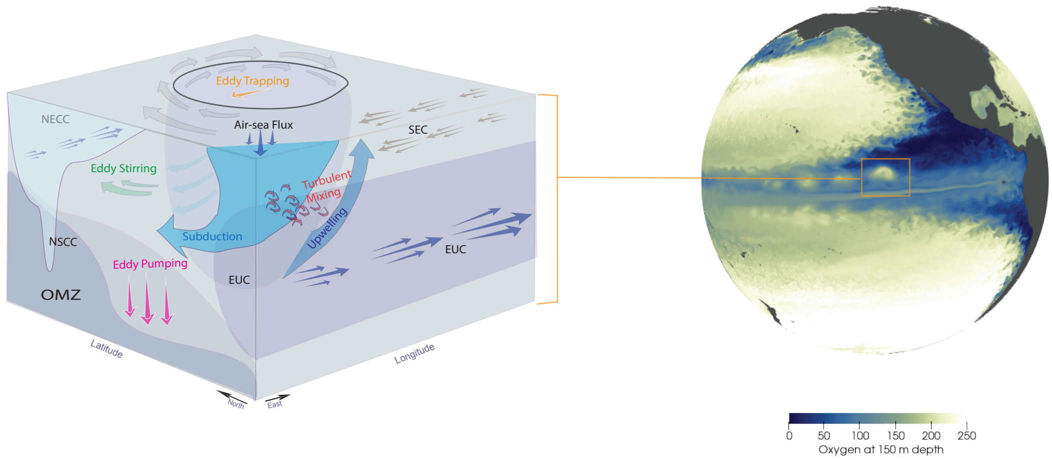

Figure 13. Summary of physical processes involved in the vortex oxygenation of the upper equatorial Pacific.

ral and spatial resolution are necessary to examine these TIV effects in more detail, and explore their imprints on the mean state and large scale ventilation of oxygen in the upper tropical Pacific.

The role of TIV-induced upwelling and subduction is especially of interest due to their potential role in facilitating oxygen supply from the mixed layer to the upper thermocline. These vertical exchanges are likely underestimated in CESM-HR due to the strong sensitivity of ageostrophic vertical velocities associated with frontogenesis on model resolution (Marchesiello et al., 2011). Vertical mixing associated with TIVs is also sensitive to the model mixing scheme (Holmes & Thomas, 2015), warranting a closer examination of these TIV effects across models of different resolution and subgrid mixing parameterizations. Other processes arising from eddy-wind interactions (e.g. Eddy-induced Ekman suction), are also known to influence biogeochemical processes (McGillicuddy, 2016; Whitt, Lévy, & Taylor, 2017; Whitt, Taylor, & Lévy, 2017). These are expected to play less of a critical role compared to the effects of eddy pumping and subduction induced by TIVs, and are the subject of future work using higher resolution simulations.

The seasonal modulation of the equatorial Pacific hypoxic depth by TIVs has important implications for marine ecosystems. TIVs not only bring about more primary productivity and colder waters along their passage, but also offer an oxygenated respite amidst largely hypoxic conditions at depth. This oxygenation coincides with the highest O_2 background concentrations associated with the seasonal cycle. Their impacts on the equatorial heat and oxygen budgets thus have relevance for understanding drivers of metabolic rates at the mesoscale (Deutsch et al., 2020), as well as characterizing the dynamics of diurnal vertical zooplankton migrations and vertical foraging ranges of larger fauna (Mislan et al., 2017; Ryan et al., 2017).

Our findings also have relevance for understanding model biases in this region. Model submissions to the most recent climate model intercomparison project (CMIP6) show OMZ biases that persist from previous model generations (Cabré et al., 2015; Kwiatkowski et al., 2020). Recent studies point to deficiencies in simulating the EUC as a major driver for these biases (Duteil et al., 2014; Busecke et al., 2019). We outline here a potentially additional source of bias associated with TIVs. In particular, the eddy pumping and subduction effects of TIVs is subdued at the 1° configuration, as expected from unresolved submesoscale and poorly resolved TIV features at coarse resolutions (Marchesiello et al., 2011), which impacts the depth of the simulated NTP OMZ and volume of the equatorial oxygenated tongue.

While mesoscale eddies have long been known to have a major and regionally-distinct influence on chlorophyll distributions (McGillicuddy, 2016), their biogeochemical impacts on O_2 have only recently been explored (Resplandy et al., 2012; Thomsen et al., 2016; Karstensen et al., 2015; Frenger et al., 2018). Recent observational and modeling studies of mesoscale eddy effects on O_2 have focused largely on the low-O_2 signature of ACMEs (Karstensen et al., 2015; Schütte et al., 2016), and their impacts on the OMZs off EBUS (Thomsen et al., 2016; Frenger et al., 2018). In contrast, TIVs lead to enhanced oxygenation of the upper ocean and a deepening of hypoxic depth along their trajectories. A driving difference in the O_2 signatures of these two mesoscale features likely stems from differences in their eddy core formation mechanisms. While TIV cores are formed through trapping and subduction of oxygenated upper ocean waters from the NECC, SEC and EUC shear region, eddy cores of ACMEs are formed off poleward undercurrent waters that are very low in O_2 and rich in nutrients. ACMEs deoxygenation effects are also tied to intensified respiration and weak exchange across the eddy boundary (Schütte et al., 2016; Karstensen et al., 2017), whereas this feedback seem to play a negligible role in TIVs in CESM-HR. In-situ validation of the simulated biogeochemical response to TIV perturbations in the equatorial Pacific as well as a model intercomparison of the biogeochemical responses to TIVs are needed to test the role of biogeochemical feedbacks during TIV events.

Given the large TIV effects on upper equatorial Pacific oxygen shown in CESM-HR, a natural next step is to find and examine these features in the real ocean. While enhanced coverage by BGC-Argo floats under the new Tropical Pacific Observing System will provide improved observational constraints on the O_2 balance in this region, dedicated process studies using gliders and other targeted in-situ measurements are needed to characterize the complex spatial patterns associated with TIVs effects on biogeochemical tracers (Archer et al., 1997; Menkes et al., 2002; Strutton et al., 2011). In turn, the TIV effects simulated here have important implications for designing monitoring networks in the tropical Pacific. In particular, resolving the large temporal O_2 variability induced by TIVs through deploying BGC-equipped autonomous vehicles and O_2 sensors on TPOS moorings are needed to complement the BGC-Argo float measurements.

An analogous modulation of the OMZ extent by TIVs is also likely on interannual timescales due to the sensitivity of TIV activity to ENSO (Zheng et al., 2016). Enhanced current shear during La Niña generates more frequent vortices, which is expected to lead to a more oxygenated upper equatorial Pacific, while fewer TIVs during El Niño are likely to drive a shoaling of the OMZ, thus compensating for ENSO-driven changes in respiration rates and the oxygen content in this region (Ito & Deutsch, 2013). Such a mechanism would lead to opposite changes from our current understanding of how the OMZs respond to ENSO (Ito & Deutsch, 2013; Eddebbar et al., 2017; Leung et al., 2019). Similarly, changes in the equatorial jets strength and shear due to multidecadal climate variability is also likely to influence O_2 trends through modulating TIV frequency on longer timescales. Predicting how OMZs will respond to anthropogenic warming will require a deeper understanding of advective and mixing processes governing the OMZ structure and ventilation (Oschlies et al., 2018), and in particular their modulation by mesoscale and submesoscale effects as the mixed layer shoals and stratification increases.

Acknowledgments

The authors acknowledge support from the National Science Foundation OCE grant number 1948599. We also acknowledge high-performance computing support from Cheyenne provided by NCAR's Computational and Information Systems Laboratory, sponsored by NSF. DBW also acknowledges support from NOAA Climate Program Office contract NA18OAR4310408 and the NASA research and analysis program. We thank Sean Haney, Anna-Lena Deppenmeier, and Deepak Cherian for useful discussions. We also acknowledge the xarray (Hoyer & Hamman, 2017), Dask (Rocklin, 2015), xgcm (Abernathey et al., 2021), and Parcels (Delandmeter & Van Sebille, 2019) Python packages for facilitating the analysis of this work. The CESM model code is available at `https://www.cesm.ucar.edu/models`. The Parcels code is available at https://github.com/OceanParcels/parcels. Velocity data from the NOAA Global Drifter Program can be found here: `https://www.aoml.noaa.gov/phod/gdp/mean_velocity.php`. Oxygen data from the CSIRO Atlas can be found here: `http://www.marine.csiro.au/~dunn/cars2009/`. Code and data used in this work are available on zenodo at `https://doi.org/10.5281/zenodo.5266337` and `https://doi.org/10.5281/zenodo.5254068`.

References

Abernathey, R., Busecke, J., Smith, T., Banihirwe, A., jdldeauna, Bot, S., ... Rath, W. (2021, May). *xgcm/xgcm: v0.5.2.* Zenodo. Retrieved from `https://doi.org/10.5281/zenodo.4821276` doi: 10.5281/zenodo.4821276

Archer, D., Aiken, J., Balch, W., Barber, D., Dunne, J., Flament, P., ... others (1997). A meeting place of great ocean currents: shipboard observations of a convergent front at 2 n in the pacific. *Deep Sea Research Part II: Topical Studies in Oceanography*, *44*(9-10), 1827–1849.

Bettencourt, J. H., López, C., Hernández-García, E., Montes, I., Sudre, J., Dewitte, B., ... Garçon, V. (2015). Boundaries of the peruvian oxygen minimum zone shaped by coherent mesoscale dynamics. *Nature Geoscience*, *8*(12), 937.

Brandt, P., Bange, H. W., Banyte, D., Dengler, M., Didwischus, S.-H., Fischer, T., ... Visbeck, M. (2015). On the role of circulation and mixing in the ventilation of oxygen minimum zones with a focus on the eastern tropical north atlantic. *Biogeosciences (BG)*, *12*, 489–512.

Busecke, J. J., Resplandy, L., & Dunne, J. P. (2019). The equatorial undercurrent and the oxygen minimum zone in the pacific. *Geophysical Research Letters*, *46*(12), 6716–6725.

Cabré, A., Marinov, I., Bernardello, R., & Bianchi, D. (2015). Oxygen minimum zones in the tropical pacific across cmip5 models: mean state differences and climate change trends. *Biogeosciences*, *12*(18), 5429–5454.

Chelton, D. B., DeSzoeke, R. A., Schlax, M. G., El Naggar, K., & Siwertz, N. (1998). Geographical variability of the first baroclinic rossby radius of deformation. *Journal of Physical Oceanography*, *28*(3), 433–460.

Cherian, D., Whitt, D., Holmes, R., Lien, R.-C., Bachman, S., & Large, W. (2021). Off-equatorial deep-cycle turbulence forced by tropical instability waves in the equatorial pacific. *Journal of Physical Oceanography*.

Cox, M. D. (1980). Generation and propagation of 30-day waves in a numerical model of the pacific. *Journal of Physical Oceanography*, *10*(8), 1168–1186.

Delandmeter, P., & Van Sebille, E. (2019). The parcels v2. 0 lagrangian framework: new field interpolation schemes. *Geoscientific Model Development*, *12*(8), 3571–3584.

Deppenmeier, A.-L., Bryan, F. O., Kessler, W., & Thompson, L. (2021). Modulation of cross-isothermal velocities with enso in the tropical pacific cold tongue. *Journal of Physical Oceanography*.

Deutsch, C., Penn, J. L., & Seibel, B. (2020). Metabolic trait diversity shapes marine biogeography. *Nature*, *585*(7826), 557–562.

Dunne, J. P., Murray, J. W., Rodier, M., & Hansell, D. A. (2000). Export flux in the western and central equatorial pacific: zonal and temporal variability. *Deep Sea Research Part I: Oceanographic Research Papers*, *47*(5), 901–936.

Duteil, O., Schwarzkopf, F. U., Böning, C. W., & Oschlies, A. (2014). Major role of the equatorial current system in setting oxygen levels in the eastern tropical atlantic ocean: A high-resolution model study. *Geophysical Research Letters*,

41(6), 2033–2040.
Dutrieux, P., Menkes, C. E., Vialard, J., Flament, P., & Blanke, B. (2008). Lagrangian study of tropical instability vortices in the atlantic. *Journal of Physical Oceanography*, *38*(2), 400–417.
Eddebbar, Y. A., Long, M. C., Resplandy, L., Rödenbeck, C., Rodgers, K. B., Manizza, M., & Keeling, R. F. (2017). Impacts of enso on air-sea oxygen exchange: Observations and mechanisms. *Global Biogeochemical Cycles*, *31*(5), 901–921.
Evans, W., Strutton, P. G., & Chavez, F. P. (2009). Impact of tropical instability waves on nutrient and chlorophyll distributions in the equatorial pacific. *Deep Sea Research Part I: Oceanographic Research Papers*, *56*(2), 178–188.
Flament, P. J., Kennan, S. C., Knox, R. A., Niiler, P. P., & Bernstein, R. L. (1996). The three-dimensional structure of an upper ocean vortex in the tropical pacific ocean. *Nature*, *383*(6601), 610.
Fox-Kemper, B., Danabasoglu, G., Ferrari, R., Griffies, S., Hallberg, R., Holland, M., ... Samuels, B. (2011). Parameterization of mixed layer eddies. iii: Implementation and impact in global ocean climate simulations. *Ocean Modelling*, *39*(1-2), 61–78.
Frenger, I., Bianchi, D., Stührenberg, C., Oschlies, A., Dunne, J., Deutsch, C., ... Schütte, F. (2018). Biogeochemical role of subsurface coherent eddies in the ocean: Tracer cannonballs, hypoxic storms, and microbial stewpots? *Global Biogeochemical Cycles*, *32*(2), 226–249.
Gallo, N., & Levin, L. (2016). Fish ecology and evolution in the world's oxygen minimum zones and implications of ocean deoxygenation. In *Advances in marine biology* (Vol. 74, pp. 117–198). Elsevier.
Garcia, H. E., Boyer, T. P., Levitus, S., Locarnini, R. A., & Antonov, J. (2005). On the variability of dissolved oxygen and apparent oxygen utilization content for the upper world ocean: 1955 to 1998. *Geophysical Research Letters*, *32*(9).
Gent, P. R., & Mcwilliams, J. C. (1990). Isopycnal mixing in ocean circulation models. *Journal of Physical Oceanography*, *20*(1), 150–155.
Gorgues, T., Menkes, C., Aumont, O., Vialard, J., Dandonneau, Y., & Bopp, L. (2005). Biogeochemical impact of tropical instability waves in the equatorial pacific. *Geophysical Research Letters*, *32*(24).
Gouretski, V., & Koltermann, K. P. (2004). Woce global hydrographic climatology. *Berichte des BSH*, *35*, 1–52.
Griffies, S. M., Biastoch, A., BÃ¶ning, C., Bryan, F., Danabasoglu, G., Chassignet, E. P., ... Yin, J. (2009). Coordinated ocean-ice reference experiments (cores). *Ocean modelling*, *26*(1-2), 1–46.
Harrison, C. S., Long, M. C., Lovenduski, N. S., & Moore, J. K. (2018). Mesoscale effects on carbon export: a global perspective. *Global Biogeochemical Cycles*, *32*(4), 680–703.
Holmes, R., McGregor, S., Santoso, A., & England, M. H. (2019). Contribution of tropical instability waves to enso irregularity. *Climate Dynamics*, *52*(3-4), 1837–1855.
Holmes, R., & Thomas, L. (2015). The modulation of equatorial turbulence by tropical instability waves in a regional ocean model. *Journal of Physical Oceanography*, *45*(4), 1155–1173.
Holmes, R., Thomas, L., Thompson, L., & Darr, D. (2014). Potential vorticity dynamics of tropical instability vortices. *Journal of physical oceanography*, *44*(3), 995–1011.
Hoyer, S., & Hamman, J. (2017). xarray: N-D labeled arrays and datasets in Python. *Journal of Open Research Software*, *5*(1). Retrieved from `http://doi.org/10.5334/jors.148` doi: 10.5334/jors.148
Hurrell, J. W., Holland, M. M., Gent, P. R., Ghan, S., Kay, J. E., Kushner, P. J., ... Marshall, S. (2013). The community earth system model: a framework for collaborative research. *Bulletin of the American Meteorological Society*, *94*(9),

1339–1360.
Inoue, R., Lien, R.-C., Moum, J. N., Perez, R. C., & Gregg, M. C. (2019). Variations of equatorial shear, stratification, and turbulence within a tropical instability wave cycle. *Journal of Geophysical Research: Oceans*, *124*(3), 1858–1875.
Ito, T., & Deutsch, C. (2013). Variability of the oxygen minimum zone in the tropical north pacific during the late twentieth century. *Global Biogeochemical Cycles*, *27*(4), 1119–1128.
Ito, T., Minobe, S., Long, M. C., & Deutsch, C. (2017). Upper ocean o2 trends: 1958–2015. *Geophysical Research Letters*, *44*(9), 4214–4223.
Johnson, G. C., Sloyan, B. M., Kessler, W. S., & McTaggart, K. E. (2002). Direct measurements of upper ocean currents and water properties across the tropical pacific during the 1990s. *Progress in Oceanography*, *52*(1), 31–61.
Karstensen, J., Fiedler, B., Schütte, F., Brandt, P., Körtzinger, A., Fischer, G., ... Wallace, D. W. (2015). Open ocean dead zones in the tropical north atlantic ocean. *Biogeosciences (BG)*, *12*, 2597–2605.
Karstensen, J., Schütte, F., Pietri, A., Krahmann, G., Fiedler, B., Grundle, D., ... others (2017). Upwelling and isolation in oxygen-depleted anticyclonic modewater eddies and implications for nitrate cycling. *Biogeosciences (BG)*, *14*(8), 2167–2181.
Karstensen, J., Stramma, L., & Visbeck, M. (2008). Oxygen minimum zones in the eastern tropical atlantic and pacific oceans. *Progress in Oceanography*, *77*(4), 331–350.
Keeling, R. F., Körtzinger, A., & Gruber, N. (2010). Ocean deoxygenation in a warming world. *Annual review of marine science*, *2*, 199–229.
Kennan, S. C., & Flament, P. J. (2000). Observations of a tropical instability vortex. *Journal of Physical Oceanography*, *30*(9), 2277–2301.
Kwiatkowski, L., Torres, O., Bopp, L., Aumont, O., Chamberlain, M., Christian, J. R., ... others (2020). Twenty-first century ocean warming, acidification, deoxygenation, and upper-ocean nutrient and primary production decline from cmip6 model projections. *Biogeosciences*, *17*(13), 3439–3470.
Large, W., & Yeager, S. (2009). The global climatology of an interannually varying air–sea flux data set. *Climate dynamics*, *33*(2-3), 341–364.
Large, W. G., McWilliams, J. C., & Doney, S. C. (1994). Oceanic vertical mixing: A review and a model with a nonlocal boundary layer parameterization. *Reviews of Geophysics*, *32*(4), 363–403.
Large, W. G., & Yeager, S. G. (2004). *Diurnal to decadal global forcing for ocean and sea-ice models: The data sets and flux climatologies.* National Center for Atmospheric Research Boulder.
Laurindo, L. C., Mariano, A. J., & Lumpkin, R. (2017). An improved near-surface velocity climatology for the global ocean from drifter observations. *Deep Sea Research Part I: Oceanographic Research Papers*, *124*, 73–92.
Legeckis, R. (1977). Long waves in the eastern equatorial pacific ocean: A view from a geostationary satellite. *Science*, *197*(4309), 1179–1181.
Lehodey, P., Murtugudde, R., & Senina, I. (2010). Bridging the gap from ocean models to population dynamics of large marine predators: a model of mid-trophic functional groups. *Progress in Oceanography*, *84*(1-2), 69–84.
Lehodey, P., Senina, I., Calmettes, B., Hampton, J., & Nicol, S. (2013). Modelling the impact of climate change on pacific skipjack tuna population and fisheries. *Climatic Change*, *119*(1), 95–109.
Leung, S., Thompson, L., McPhaden, M. J., & Mislan, K. (2019). Enso drives near-surface oxygen and vertical habitat variability in the tropical pacific. *Environmental Research Letters*.
Lien, R.-C., d'Asaro, E. A., & Menkes, C. E. (2008). Modulation of equatorial turbulence by tropical instability waves. *Geophysical Research Letters*, *35*(24).

Long, M. C., Deutsch, C., & Ito, T. (2016). Finding forced trends in oceanic oxygen. *Global Biogeochemical Cycles*, *30*(2), 381–397.

Long, M. C., Lindsay, K., Peacock, S., Moore, J. K., & Doney, S. C. (2013). Twentieth-century oceanic carbon uptake and storage in cesm1 (bgc). *Journal of Climate*, *26*(18), 6775–6800.

Luyten, J., Pedlosky, J., & Stommel, H. (1983). The ventilated thermocline. *Journal of Physical Oceanography*, *13*(2), 292–309.

Marchesiello, P., Capet, X., Menkes, C., & Kennan, S. C. (2011). Submesoscale dynamics in tropical instability waves. *Ocean Modelling*, *39*(1-2), 31–46.

Margolskee, A., Frenzel, H., Emerson, S., & Deutsch, C. (2019). Ventilation pathways for the north pacific oxygen deficient zone. *Global Biogeochemical Cycles*, *33*(7), 875–890.

Martin, A. P., & Richards, K. J. (2001). Mechanisms for vertical nutrient transport within a north atlantic mesoscale eddy. *Deep Sea Research Part II: Topical Studies in Oceanography*, *48*(4-5), 757–773.

McGillicuddy, D. J. (2016). Mechanisms of physical-biological-biogeochemical interaction at the oceanic mesoscale. *Annual Review of Marine Science*, *8*(1), 125-159. Retrieved from `https://doi.org/10.1146/annurev-marine-010814-015606` (PMID: 26359818) doi: 10.1146/annurev-marine-010814-015606

Ménard, F., Fonteneau, A., Gaertner, D., Nordstrom, V., Stéquert, B., & Marchal, E. (2000). Exploitation of small tunas by a purse-seine fishery with fish aggregating devices and their feeding ecology in an eastern tropical atlantic ecosystem. *ICES Journal of Marine Science*, *57*(3), 525–530.

Menkes, C. E., Kennan, S. C., Flament, P., Dandonneau, Y., Masson, S., Biessy, B., … Herbland, A. (2002). A whirling ecosystem in the equatorial atlantic. *Geophysical Research Letters*, *29*(11), 48–1.

Menkes, C. E., Vialard, J. G., Kennan, S. C., Boulanger, J.-P., & Madec, G. V. (2006). A modeling study of the impact of tropical instability waves on the heat budget of the eastern equatorial pacific. *Journal of Physical Oceanography*, *36*(5), 847–865.

Mislan, K., Deutsch, C. A., Brill, R. W., Dunne, J. P., & Sarmiento, J. L. (2017). Projections of climate-driven changes in tuna vertical habitat based on species-specific differences in blood oxygen affinity. *Global change biology*, *23*(10), 4019–4028.

Moore, J. K., Lindsay, K., Doney, S. C., Long, M. C., & Misumi, K. (2013). Marine ecosystem dynamics and biogeochemical cycling in the community earth system model [cesm1 (bgc)]: Comparison of the 1990s with the 2090s under the rcp4. 5 and rcp8. 5 scenarios. *Journal of Climate*, *26*(23), 9291–9312.

Morlière, A., Lebouteiller, A., & Citeau, J. (1994). Tropical instability waves in the atlantic-ocean-a contributor to biological processes. *Oceanologica Acta*, *17*(6), 585–596.

Moum, J., Lien, R.-C., Perlin, A., Nash, J., Gregg, M., & Wiles, P. (2009). Sea surface cooling at the equator by subsurface mixing in tropical instability waves. *Nature Geoscience*, *2*(11), 761–765.

Okubo, A. (1970). Horizontal dispersion of floatable particles in the vicinity of velocity singularities such as convergences. In *Deep sea research and oceanographic abstracts* (Vol. 17, pp. 445–454).

Oschlies, A., Brandt, P., Stramma, L., & Schmidtko, S. (2018). Drivers and mechanisms of ocean deoxygenation. *Nature geoscience*, *11*(7), 467.

Philander, S. (1976). Instabilities of zonal equatorial currents. *Journal of Geophysical Research*, *81*(21), 3725–3735.

Redi, M. H. (1982). Oceanic isopycnal mixing by coordinate rotation. *Journal of Physical Oceanography*, *12*(10), 1154–1158.

Resplandy, L., Lévy, M., Bopp, L., Echevin, V., Pous, S., Sarma, V., & Kumar, D. (2012). Controlling factors of the omz in the arabian sea. *Biogeosciences*

Discussions, *9*(5).

Ridgway, K., Dunn, J., & Wilkin, J. (2002). Ocean interpolation by four-dimensional weighted least squares—application to the waters around australasia. *Journal of atmospheric and oceanic technology*, *19*(9), 1357–1375.

Rocklin, M. (2015). Dask: Parallel computation with blocked algorithms and task scheduling. In K. Huff & J. Bergstra (Eds.), *Proceedings of the 14th python in science conference* (p. 130 - 136).

Ryan, J. P., Green, J. R., Espinoza, E., & Hearn, A. R. (2017). Association of whale sharks (rhincodon typus) with thermo-biological frontal systems of the eastern tropical pacific. *PLoS One*, *12*(8), e0182599.

Schmidtko, S., Stramma, L., & Visbeck, M. (2017). Decline in global oceanic oxygen content during the past five decades. *Nature*, *542*(7641), 335.

Schütte, F., Karstensen, J., Krahmann, G., Hauss, H., Fiedler, B., Brandt, P., ... Körtzinger, A. (2016). Characterization of "dead-zone" eddies in the eastern tropical north atlantic. *Biogeosciences*, *13*(20), 5865–5881.

Small, R. J., Bacmeister, J., Bailey, D., Baker, A., Bishop, S., Bryan, F., ... Vertenstein, M. (2014). A new synoptic scale resolving global climate simulation using the community earth system model. *Journal of Advances in Modeling Earth Systems*, *6*(4), 1065–1094.

Smith, R., Jones, P., Briegleb, B., Bryan, F., Danabasoglu, G., Dennis, J., ... Hecht, M. (2010). The parallel ocean program (pop) reference manual: ocean component of the community climate system model (ccsm) and community earth system model (cesm). *Rep. LAUR-01853*, *141*, 1–140.

Stramma, L., Johnson, G. C., Firing, E., & Schmidtko, S. (2010). Eastern pacific oxygen minimum zones: Supply paths and multidecadal changes. *Journal of Geophysical Research: Oceans*, *115*(C9).

Stramma, L., Schmidtko, S., Levin, L. A., & Johnson, G. C. (2010). Ocean oxygen minima expansions and their biological impacts. *Deep Sea Research Part I: Oceanographic Research Papers*, *57*(4), 587–595.

Strutton, P. G., Palacz, A. P., Dugdale, R. C., Chai, F., Marchi, A., Parker, A. E., ... Wilkerson, F. P. (2011). The impact of equatorial pacific tropical instability waves on hydrography and nutrients: 2004-2005. *Deep Sea Research Part II: Topical Studies in Oceanography*, *58*(3-4), 284–295.

Strutton, P. G., Ryan, J. P., & Chavez, F. P. (2001). Enhanced chlorophyll associated with tropical instability waves in the equatorial pacific. *Geophysical Research Letters*, *28*(10), 2005–2008.

Sverdrup, H. (1938). On the explanation of the oxygen minima and maxima in the oceans. *ICES Journal of Marine Science*, *13*(2), 163–172.

Thomsen, S., Kanzow, T., Krahmann, G., Greatbatch, R. J., Dengler, M., & Lavik, G. (2016). The formation of a subsurface anticyclonic eddy in the p eru-c hile u ndercurrent and its impact on the near-coastal salinity, oxygen, and nutrient distributions. *Journal of Geophysical Research: Oceans*, *121*(1), 476–501.

Ubelmann, C., & Fu, L.-L. (2011). Vorticity structures in the tropical pacific from a numerical simulation. *Journal of physical oceanography*, *41*(8), 1455–1464.

Van Sebille, E., Griffies, S. M., Abernathey, R., Adams, T. P., Berloff, P., Biastoch, A., ... Zika, J. D. (2018a). Lagrangian ocean analysis: Fundamentals and practices. *Ocean Modelling*, *121*, 49–75.

Van Sebille, E., Griffies, S. M., Abernathey, R., Adams, T. P., Berloff, P., Biastoch, A., ... others (2018b). Lagrangian ocean analysis: Fundamentals and practices. *Ocean Modelling*, *121*, 49–75.

Vaquer-Sunyer, R., & Duarte, C. M. (2008). Thresholds of hypoxia for marine biodiversity. *Proceedings of the National Academy of Sciences*, *105*(40), 15452–15457.

Wang, M., Du, Y., Qiu, B., Xie, S.-P., & Feng, M. (2019). Dynamics on seasonal variability of eke associated with tiws in the eastern equatorial pacific ocean.

Journal of Physical Oceanography, *49*(6), 1503–1519.
Weiss, J. (1991). The dynamics of enstrophy transfer in two-dimensional hydrodynamics. *Physica D: Nonlinear Phenomena*, *48*(2-3), 273–294.
Whitt, D., Lévy, M., & Taylor, J. R. (2017). Low-frequency and high-frequency oscillatory winds synergistically enhance nutrient entrainment and phytoplankton at fronts. *Journal of Geophysical Research: Oceans*, *122*(2), 1016–1041.
Whitt, D., Taylor, J. R., & Lévy, M. (2017). Synoptic-to-planetary scale wind variability enhances phytoplankton biomass at ocean fronts. *Journal of Geophysical Research: Oceans*, *122*(6), 4602–4633.
Willett, C. S., Leben, R. R., & Lavín, M. F. (2006). Eddies and tropical instability waves in the eastern tropical pacific: A review. *Progress in Oceanography*, *69*(2-4), 218–238.
Wyrtki, K. (1962). The oxygen minima in relation to ocean circulation. In *Deep sea research and oceanographic abstracts* (Vol. 9, pp. 11–23).
Zheng, S., Feng, M., Du, Y., Cheng, X., & Li, J. (2016). Annual and interannual variability of the tropical instability vortices in the equatorial eastern pacific observed from lagrangian surface drifters. *Journal of Climate*, *29*(24), 9163–9177.